Article

Bragg Resonance of Water Waves by Multiple Permeable Thin Barriers over Periodic Breakwaters

Chang-Thi Tran [1], Chitsan Lin [1,2,3] and Chia-Cheng Tsai [4,5,*]

1   Institute of Aquatic Science and Technology, National Kaohsiung University of Science and Technology, Kaohsiung 811213, Taiwan
2   Ph.D. Program in Maritime Science and Technology, College of Maritime, National Kaohsiung University of Science and Technology, Kaohsiung 811213, Taiwan
3   Department of Marine Environmental Engineering, National Kaohsiung University of Science and Technology Kaohsiung, Kaohsiung 811213, Taiwan
4   Bachelor Degree Program in Ocean Engineering and Technology, National Taiwan Ocean University, Keelung 202301, Taiwan
5   Center of Excellence for Ocean Engineering, National Taiwan Ocean University, Keelung 202301, Taiwan
*   Correspondence: cctsai@mail.ntou.edu.tw

Abstract: In this study, the Bragg resonance of water waves scattered by multiple permeable thin barriers over a series of periodic breakwaters was solved by employing the eigenfunction matching method (EMM). The geometrical configuration was divided into multiple shelves separated by steps, on which thin permeable barriers were implemented. The solution was approximated using eigenfunctions with unknown coefficients that were considered as the amplitudes of the water waves for each shelf. The conservations of mass and momentum were then applied to form a system of linear equations, which was sequentially solved by a sparse-matrix solver. The proposed method degenerates to traditional EMM formulations if thin barriers, the permeability of the barrier, or bottom undulations are not considered. The validity of the suggested method was examined based on the results in the literature. Bragg resonances by bottom-standing, surface-piecing, and fully submerged permeable barriers over a series of periodic trapezoidal or half-cosine breakwaters were studied. In addition, the breakwater amplitudes, permeable parameters of the barriers, and incident angles of water wave scattering by different types of periodic breakwaters were discussed.

Keywords: Bragg resonance; periodic breakwaters; water wave scattering; eigenfunction matching method; permeable barrier

1. Introduction

Water waves undergo many phenomena, principally from the assembled influences of undulation bottom topographies, interference with artificial coastal foundations, and nonlinear interactions between different harmonic components of waves traveling landward. Coastal structures such as bulkheads, breakwaters, groins, and seawalls are used to diminish wave impact and protect the shoreline. Along with coastal protection, these coastal structures are used as artificial breeding grounds for sea animals and play an essential role in the sustainable development of a healthy ecosystem in harbors. Therefore, material involvement and thin permeable barriers could be valuable structures for reducing construction costs. Moreover, this is preferred in many circumstances. For example, a bottom-standing barrier can be used in long-wave environments. Alternatively, a surface-piercing barrier can be used under special conditions, such as poor soil foundations.

The issue of water wave scattering by an impermeable barrier over a flat bottom was examined in the previous studies [1–5]. Ursell [6] researched oblique water waves passing through a thin barrier in deep water. Das et al. [7] studied the impact of multiple impermeable thin barriers on the scattering of water waves. To further dissipate wave

energy, the issues of permeable structures that are thin barriers have been studied [8–11]. By solving integral equations, Macaskill [12] considered waves scattered by a single permeable barrier at a finite water depth.

Numerical solutions have been widely used to investigate the interaction of water waves with structures. The eigenfunction matching method (EMM) was examined by Takano [13] to evaluate scattered water waves with an upraised rectangular sill. Following this approach, Newman [14] considered the problem of propagating waves past long symmetrical obstacles. Subsequently, Mei and Black [15] applied the EMM to solve surface waves typically incident on a rectangular obstacle in a channel of finite depth. EMM was then used to study the problems of oblique wave scattering by rectangular trenches [16,17]. In the case of waves propagated by undulating topography, Devillard et al. [18], O'Hare and Davies [19], and Tsai et al. [20–22] almost exclusively focused on decomposed bottom profiles in the concept that contain a series of flat shelves divided into multiple steps and solved it using the EMM. Losada et al. [2] and Abul-Azm [5] employed methods of matched eigenfunction expansion to investigate analytical solutions for the diffractions of oblique waves with different configurations of thin vertical barriers. The matched eigenfunction expansion method was used to study the context of wave interactions with vertical slotted barriers [23,24] and impermeable barriers [25].

A specific configuration by a series of periodic breakwaters is known to reflect oblique incident water waves resonantly. Bragg and Bragg [26] first discussed the occurrence of Bragg resonance phenomena, and this mechanism inspired several studies on the concept of submerged artificial bars [27–30] or natural bars [31–35]. Bragg resonance occurs when the length of the surface water wave is approximately double the ratio of adjacent breakwaters, and incident waves may be reflected in the sea. Kar, et al. [36–39] also applied the boundary element method to study the Bragg scattering of surface gravity waves by an array of trenches over undulation bottom topographies to enhance the width of the existing channels. Ting, et al. [40] examined the Bragg resonance of water waves over the permeable rippled seabed in the nearshore region. Xie [41] investigated the Bragg reflections of linear long waves over an array of trapezoidal breakwaters on a sloping seabed.

In this study, we considered the Bragg resonant reflections of water waves created by multiple thin permeable barriers over periodic breakwaters. Three configurations of permeable thin barriers were employed: bottom-standing, surface-piercing, and fully submerged barriers. In addition, we investigated the effects of two types of periodic breakwaters, that is, the trapezoidal and half-cosine breakwaters, on the resonance of Bragg scattering.

The rest of the paper is structured as follows. In Section 2, the water waves are mathematically modeled. Subsequently, an EMM solution is formulated. To validate the efficiency of the proposed EMM solution, several issues are discussed in Section 3. In Section 4, further discussions on the Bragg resonances of water wave reflections and energy loss by multiple permeable barriers over two types of periodic breakwaters are presented in detail. Finally, Section 5 provides generalized conclusions for the entire study.

2. Methodology

2.1. The Mathematical Model

The scattering of sinusoidal surface waves towards an array of periodic breakwaters with thin permeable barriers was investigated in two-dimensional coordination. The waves had amplitude $\bar{a}$, incidence angle γ, angular frequency $\sigma = 2\pi/T$, where T denotes the period of the wave, and wavelength λ. Here, the z-axis was measured vertically upward, and the x-axis was along the horizontal direction. A schematic of a series of periodic breakwaters with multiple permeable thin barriers associated with water waves is presented in Figure 1. The wave amplitude was sufficiently reduced to satisfy the theory of linear waves. The wave motion is supposed to be time-harmonic $e^{-i\sigma t}$, where $\mathbf{i}$ represents the imaginary unit of complex numbers, and t denotes the time. To facilitate the approximation of the bottom topography and thin barriers, they were discretized into

a sequence of M shelves in the interval $x_{m-1} \leq x \leq x_m$ for $m = 1, 2, \ldots, M$ with a water depth h_m. In addition, we assumed that $x_0 = -\infty$ and $x_M = \infty$. The i-th surface-piercing barrier was placed at a location $x = v_i$ with a submerged length equal to a_i. In addition, the i-th bottom-standing barrier was placed at a location $x = w_i$ with length b_i. In the following section, $a = a_i$, $v = v_i$, $b = b_i$, or $w = w_i$ if there is only one surface-piercing or bottom-standing barrier.
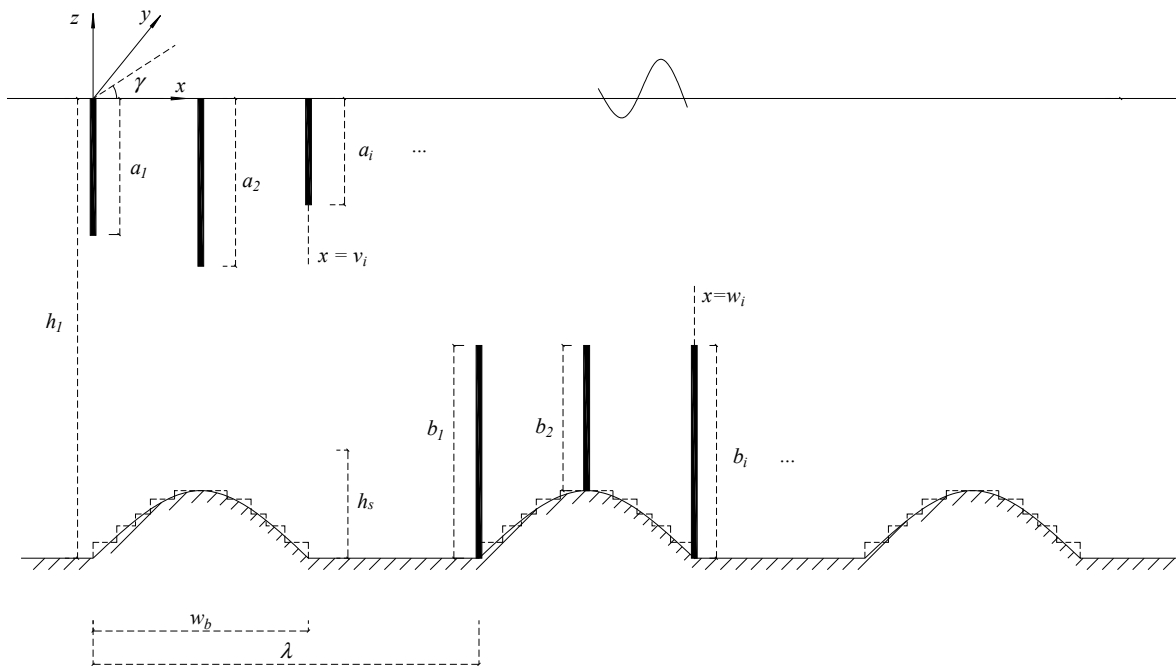

Figure 1. Schematic of water wave reflection by multiple permeable barriers over periodic breakwaters.

Let us consider a single-step separation of abrupt shelves, as depicted in Figure 2. Here, L_g and L_b are the vertical intervals of the gap and the barrier, respectively. If a barrier is absent, L_b is equal to zero. The m-th shelf in the interspace $x_{m-1} \leq x \leq x_m$, for $m = 1, 2, \ldots, M$, $\mathbf{u}_m$ represents the fluid velocity and is calculated as:

$$\mathbf{u}_m = \nabla \phi_m, \tag{1}$$

where the three-dimensional operator $\nabla = (\partial/\partial x, \partial/\partial y, \partial/\partial z)$, which concerns the Cartesian coordinate systems (x, y, z) and ϕ_m, denotes the velocity potential.

Thus, to satisfy the Laplace equation in the fluid domain:

$$\nabla^2 \phi_m = 0, \tag{2}$$

which respectively dominated the free-surface boundary conditions of kinematic and dynamic as

$$-\mathbf{i}\sigma \eta_m - \frac{\partial \phi_m}{\partial z} = 0 \tag{3}$$

and at $z = 0$,

$$-\mathbf{i}\sigma \phi_m + g\eta_m = 0 \tag{4}$$

where η_m denotes the surface elevation. Combining Equations (3) and (4), we obtain

$$\frac{\partial \phi_m}{\partial z} - \frac{\sigma^2}{g}\phi_m = 0 \text{ on } z = 0. \tag{5}$$

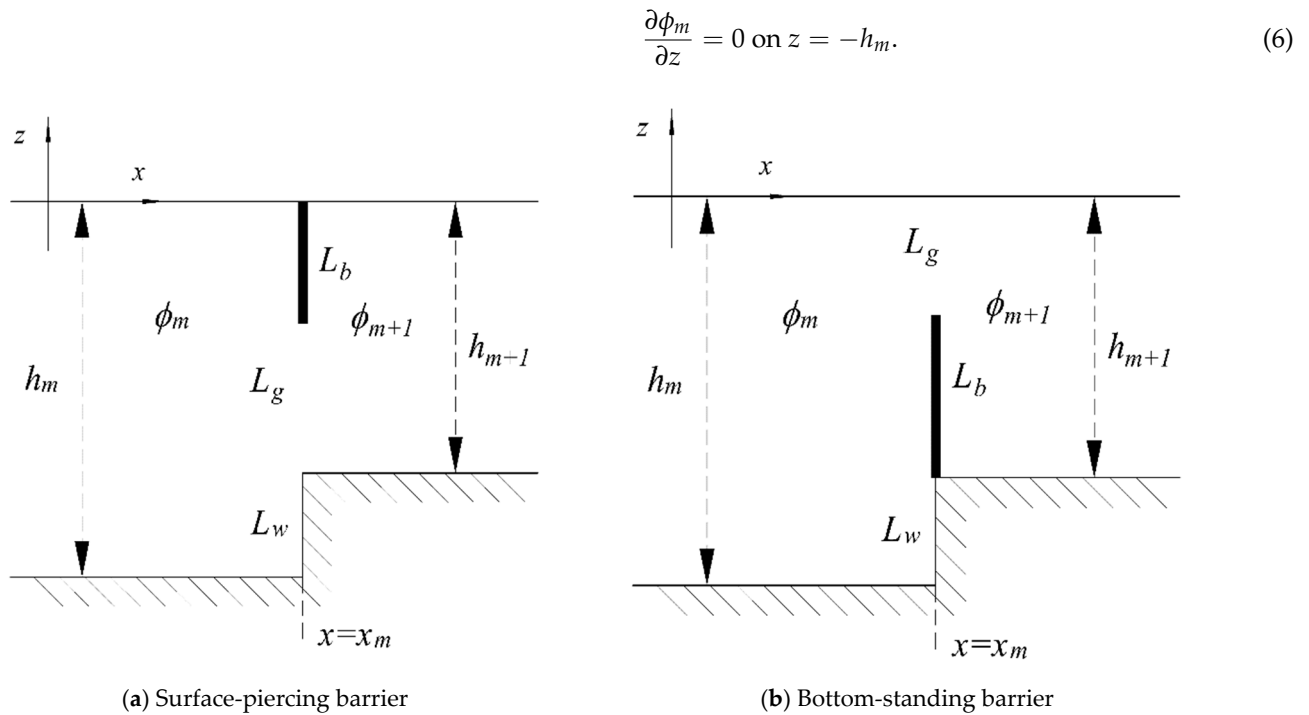In addition, the condition for the bottom boundary can be written as

$$\frac{\partial \phi_m}{\partial z} = 0 \text{ on } z = -h_m. \tag{6}$$

(**a**) Surface-piercing barrier　　　　　　(**b**) Bottom-standing barrier

Figure 2. (**a**) Surface-piercing barrier and (**b**) bottom-standing barrier for separated abrupt shelves.

Between two continuous shelves, connection conditions are required for the velocity potentials ϕ_m and ϕ_{m+1}

$$\phi_m = \phi_{m+1} \text{ for } x \in L_g, \tag{7}$$

$$\frac{\partial \phi_m}{\partial x} = \frac{\partial \phi_{m+1}}{\partial x} \text{ for } x \in L_g, \tag{8}$$

and

$$\frac{\partial \phi_m}{\partial x} = \frac{\partial \phi_{m+1}}{\partial x} = \mathbf{i}G(\phi_m - \phi_{m+1}) \text{ for } x \in L_b, \tag{9}$$

where G is the permeability parameter defined by Isaacson et al. [23]. Moreover, for a vertical wall, the condition is calculated using the following equation:

$$\frac{\partial \phi}{\partial x} = 0 \text{ for } x \in L_w \tag{10}$$

In Equation (10), ϕ consent to either ϕ_m or ϕ_{m+1}, for the waterside of the barrier, and L_w is the vertical intervals of the wall.

To make the solution uniquely solvable, the following far-field conditions must be satisfied:

$$\eta = \bar{a} \left(e^{\mathbf{i}\hat{k}_{1,0}x} + K_R e^{\mathbf{i}\theta_R} e^{-\mathbf{i}\hat{k}_{1,0}x} \right) e^{\mathbf{i}k_y y} \text{ as } x \to -\infty \tag{11}$$

and

$$\eta = \bar{a} K_T e^{\mathbf{i}\theta_T} e^{\mathbf{i}\hat{k}_{M,0}x} e^{\mathbf{i}k_y y} \text{ as } x \to \infty, \tag{12}$$

where K_R, K_T, θ_R and θ_T take the values of real numbers as the reflection and transmission coefficients conceivably further specified by $K_R e^{\mathbf{i}\theta_R}$ and $K_T e^{\mathbf{i}\theta_T}$, respectively.

In Equations (11) and (12), $\hat{k}_{M,0}$, k_y, and $\hat{k}_{1,0}$ represent the positive real wavenumbers indicated by

$$\hat{k}_{m,n} = \sqrt{k_{m,n}^2 - k_y^2} \tag{13}$$

and

$$k_y = k_{1,0} \sin \gamma, \tag{14}$$

where $k_{1,0} = 2\pi/\lambda > 0$ and $k_{M,0} > 0$ are the continuing wavenumbers, which can be established from the following dispersion relation

$$\frac{\sigma^2}{g} = k_{m,0}\tanh k_{m,0}h_m. \tag{15}$$

In Equation (13), the indices vary between $m = 1, 2, \ldots, M$ and $n = 0, 1, \ldots$ Furthermore, in Equation (13), the evanescent wavenumbers $k_{m,n}$ with $n > 0$ are expressed as

$$k_{m,n} = \mathbf{i}\kappa_{m,n}, \tag{16}$$

where $\kappa_{m,n}$ represents the n-th smallest positive root of the dispersion relation

$$\frac{\sigma^2}{g} = -\kappa_{m,n}\tan\kappa_{m,n}h_m. \tag{17}$$

2.2. Method of Solution

In accordance with the linear wave theory, for the m-th shelf, the solution of the velocity potential can be expressed as

$$\phi_m(x, y, z) = \sum_{n=0}^{N}\left(A_{m,n}\xi_{m,n}^{(1)}(x) + B_{m,n}\xi_{m,n}^{(2)}(x)\right)\zeta_{m,n}(z)e^{\mathbf{i}k_y y} \tag{18}$$

where the unknown coefficients $A_{m,n}$ and $B_{m,n}$ need to be resolved for $m = 1, 2, \ldots, M$. The factor N in Equation (18) is assumed to be the evanescent mode number. By isolating the variables, the eigenfunctions in Equation (18) can be defined as

$$\zeta_{m,n}(z) = \cosh k_{m,n}(h_m + z), \tag{19}$$

$$\xi_{m,n}^{(1)}(x) = e^{\mathbf{i}\hat{k}_{m,n}(x - \bar{x}_{m-1})}, \tag{20}$$

and

$$\xi_{m,n}^{(2)}(x) = e^{-\mathbf{i}\hat{k}_{m,n}(x - \bar{x}_m)} \tag{21}$$

with

$$\begin{cases} \bar{x}_m = x_m \\ \bar{x}_0 = \bar{x}_M = 0 \end{cases} \quad \text{for } m = 1, 2, \ldots, M - 1. \tag{22}$$

It can be observed that the solutions defined in Equations (13)–(22) satisfy Equations (2), (5), and (6): By applying Equations (7)–(12), the unknown coefficients, $A_{m,n}$ and $B_{m,n}$, can be obtained.

Hence, the EMM is applied to define the conservation of mass in Equations (8)–(10) as follows:

$$\left\langle \frac{\partial\phi_m}{\partial x}\middle|\zeta_{m,l}^{\text{larger}}\right\rangle = \left\langle \frac{\partial\phi_{m+1}}{\partial x}\middle|\zeta_{m,l}^{\text{larger}}\right\rangle \text{ for } l = 0, 1, 2, \ldots, N, \tag{23}$$

where the two-depth eigenfunctions inner product can be formulated as

$$\langle P_1|P_2\rangle = \int_{-\tilde{h}}^{0} P_1(z)P_2(x)dz \tag{24}$$

where P_1 and P_2 represent the depth eigenfunction of $\zeta_{m,n}$ with arbitrary integers m and n, respectively. In addition, $\tilde{h}$ indicates the water depth of the eigenfunction P_1. Moreover, in Equation (23), $\zeta_{m,l}^{\text{larger}}$ is derived as

$$\zeta_{m,l}^{\text{larger}} = \begin{cases} \zeta_{m,l} & \text{for } h_m > h_{m+1} \\ \zeta_{m+1,l} & \text{for } h_{m+1} > h_m. \end{cases} \tag{25}$$

In Equations (7) and (9), the conservation of momentum and the barrier condition can be expressed as:

$$\left\langle \zeta_{m,l}^{\text{smaller}} \middle| \phi_m(x_m) \right\rangle = \left\langle \zeta_{m,l}^{\text{smaller}} \middle| \phi_{m+1}(x_m) \right\rangle + \left\langle F \middle| \zeta_{m,l}^{\text{smaller}} \right\rangle \text{ for } l = 0, 1, \ldots, N, \tag{26}$$

where

$$F(z) = \frac{\partial \phi_m}{\partial x} - (\mathrm{i}G - 1)(\phi_m(x_m) - \phi_{m+1}(x_m)) \text{ for } x \in L_b, \tag{27}$$

and

$$\zeta_{m,l}^{\text{smaller}} = \begin{cases} \zeta_{m,l} & \text{for } h_m < h_{m+1} \\ \zeta_{m+1,l} & \text{for } h_{m+1} < h_m. \end{cases} \tag{28}$$

Depending on condition (4) and the far-field conditions defined in Equations (11) and (12), we can define the far-field solutions of the velocity potential as:

$$\phi_1 = -\frac{\mathrm{i}\bar{a}g}{\sigma} \frac{\cosh k_{1,0}(h_1 + z)}{\cosh k_{1,0}h_1} \left(e^{\mathrm{i}\hat{k}_{1,0}x} + K_R e^{\mathrm{i}\theta_R} e^{-\mathrm{i}\hat{k}_{1,0}x} \right) e^{\mathrm{i}k_y y} \text{ as } x \to -\infty \tag{29}$$

and

$$\phi_M = -\frac{\mathrm{i}\bar{a}g}{\sigma} \frac{\cosh k_{M,0}(h_M + z)}{\cosh k_{M,0}h_M} \left(K_T e^{\mathrm{i}\theta_T} e^{\mathrm{i}\hat{k}_{M,0}x} \right) e^{\mathrm{i}k_y y} \text{ as } x \to \infty. \tag{30}$$

Combining Equations (29) and (30) into Equation (18), the following equations are obtained:

$$B_{1,0} e^{\mathrm{i}\hat{k}_{m,n}x} = -\frac{\mathrm{i}\bar{a}K_R e^{\mathrm{i}\theta_R} g}{\sigma} \frac{1}{\cosh k_{1,0}h_1}, \tag{31}$$

$$A_{M,0} e^{-\mathrm{i}\hat{k}_{M,0}\bar{x}_{M-1}} = -\frac{\mathrm{i}\bar{a}K_T e^{\mathrm{i}\theta_T} g}{\sigma} \frac{1}{\cosh k_{M,0}h_M}, \tag{32}$$

$$A_{1,0} = -\frac{\mathrm{i}ag}{\sigma} \frac{1}{\cosh k_{1,0}h_1}, \tag{33}$$

$$A_{1,n} = 0 \text{ for } n = 1, 2, 3, \ldots, N, \tag{34}$$

and

$$B_{M,n} = 0 \text{ for } n = 0, 1, 2, \ldots, N. \tag{35}$$

Using Equation (18), Equations (23) and (26) can be rewritten as follows:

$$\sum_{n=0}^{N} \left(\mathrm{i}\hat{k}_{m,n} A_{m,n} \xi_{m,n}^{(1)}(x_m) - \mathrm{i}\hat{k}_{m,n} B_{m,n} \xi_{m,n}^{(2)}(x_m) \right) \left\langle \zeta_{m,n} | \zeta_{m,l}^{\text{larger}} \right\rangle$$
$$= \sum_{n=0}^{N} \left(\mathrm{i}\hat{k}_{m+1,n} A_{m+1,n} \xi_{m+1,n}^{(1)}(x_m) - \mathrm{i}\hat{k}_{m+1,n} B_{m+1,n} \xi_{m,n}^{(2)}(x_m) \right) \left\langle \zeta_{m+1,n} | \zeta_{m,l}^{\text{larger}} \right\rangle \tag{36}$$

and

$$\sum_{n=0}^{N} \left(A_{m,n} \xi_{m,n}^{(1)}(x_m) + B_{m,n} \xi_{m,n}^{(2)}(x_m) \right) \left\langle \zeta_{m,l}^{\text{smaller}} \middle| \zeta_{m,n} \right\rangle$$
$$= \sum_{n=0}^{N} \left(A_{m+1,n} \xi_{m,n}^{(1)}(x_m) + B_{m+1,n} \xi_{m,n}^{(2)}(x_m) \right) \left\langle \zeta_{m,l}^{\text{smaller}} \middle| \zeta_{m+1,n} \right\rangle + \left\langle F \middle| \zeta_{m,l}^{\text{smaller}} \right\rangle, \tag{37}$$

for the region of $l = 0, 1, 2, \ldots, N$ and $m = 1, 2, 3, \ldots, M - 1$. Subsequently, the EMM can be established using Equations (33)–(37), which compose $2M(N + 1)$ linear equations and are subsequently employed to determine the $2M(N + 1)$ unknown coefficients $A_{m,n}$ and $B_{m,n}$. The detailed coefficients of reflection and transmission, $K_R e^{\mathrm{i}\theta_R}$ and $K_T e^{\mathrm{i}\theta_T}$, are later determined by applying Equations (31) and (32). It must be noted that the proposed EMM formulation degenerates into the formulation to deal with the problem of water wave interactions with impermeable barriers [25] over uneven bottoms during $G = 0$. In addition,

it degenerates into the formulation of water wave scattering by breakwaters [13,20,42] if the L_b is null.

3. Results

A concise and precise description of the experimental results, their interpretation, and the experimental conclusions that can be drawn from the results have been provided in this section.

In this section, the proposed EMM is adjusted to investigate simplified problems of water wave interaction with permeable barriers over a flat bottom, periodic breakwaters, and fully submerged barriers over a flat bottom behind an otherwise undulated bottom. These results were compared with the results available in the literature.

3.1. Water Wave Interactions with a Single Permeable Barrier over Flat Bottom Topography

Initially, the suggested model was applied to solve the diffractions of water waves by a single barrier with a flat bottom, where $h_1 = h_2 = 1.0$ m. First, the interactions of water waves with a surface-piercing barrier were investigated, and the submerged length of the barrier from the free surface was $a/h_1 = 0.5$. For the case of a single permeable bottom-standing barrier, the physical dimension of the barrier lengths was $b/h_1 = 0.5$. In addition, the number of evanescent modes was set to $N = 50$ for both cases.

Figure 3a,b depict the variations in $|R|$ and $|T|$ as a function of dimensionless wavenumber $k_{1,0}h_1$ with several values of the permeable parameter G for the water wave scattered by a single permeable surface-piercing barrier and bottom-standing barrier, respectively. The general curves of $|R|$ and $|T|$ for different values of G were in good agreement with the results of Lee and Chwang [9] and Li et al. [10], respectively.
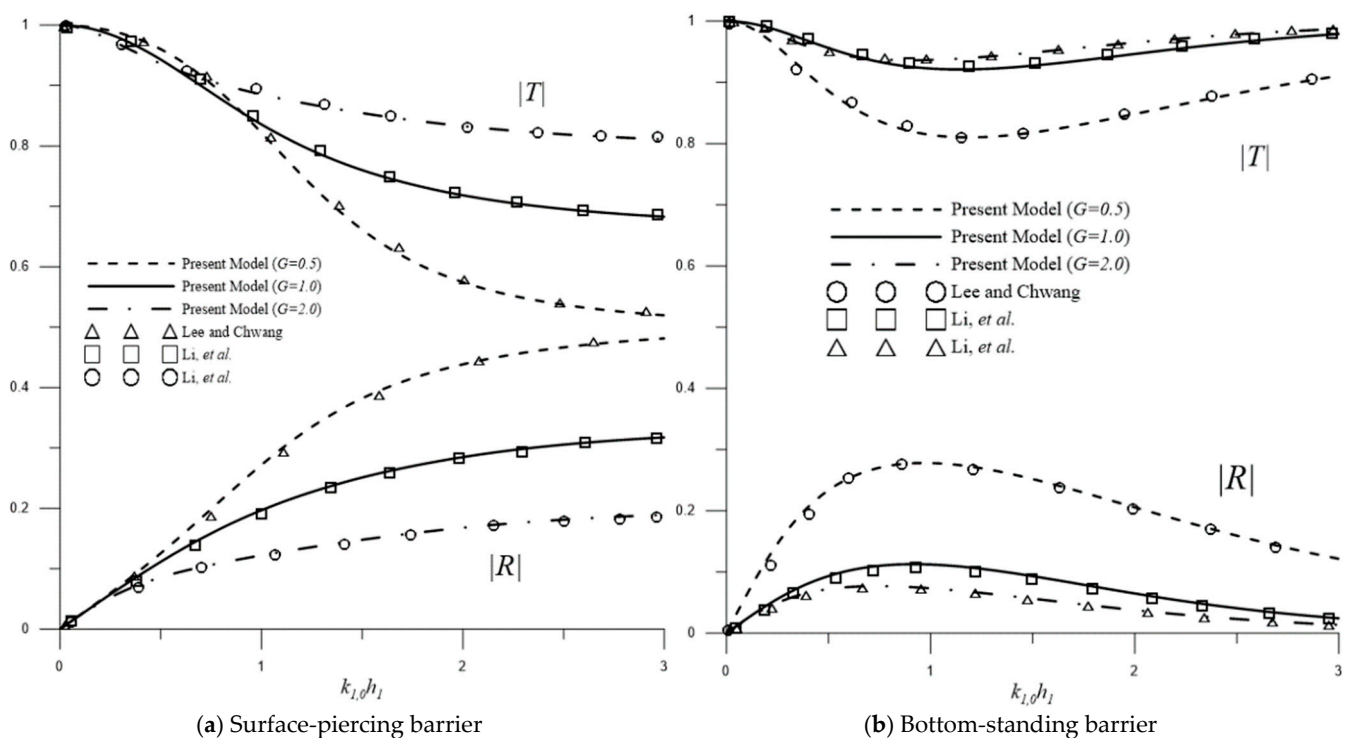

(**a**) Surface-piercing barrier
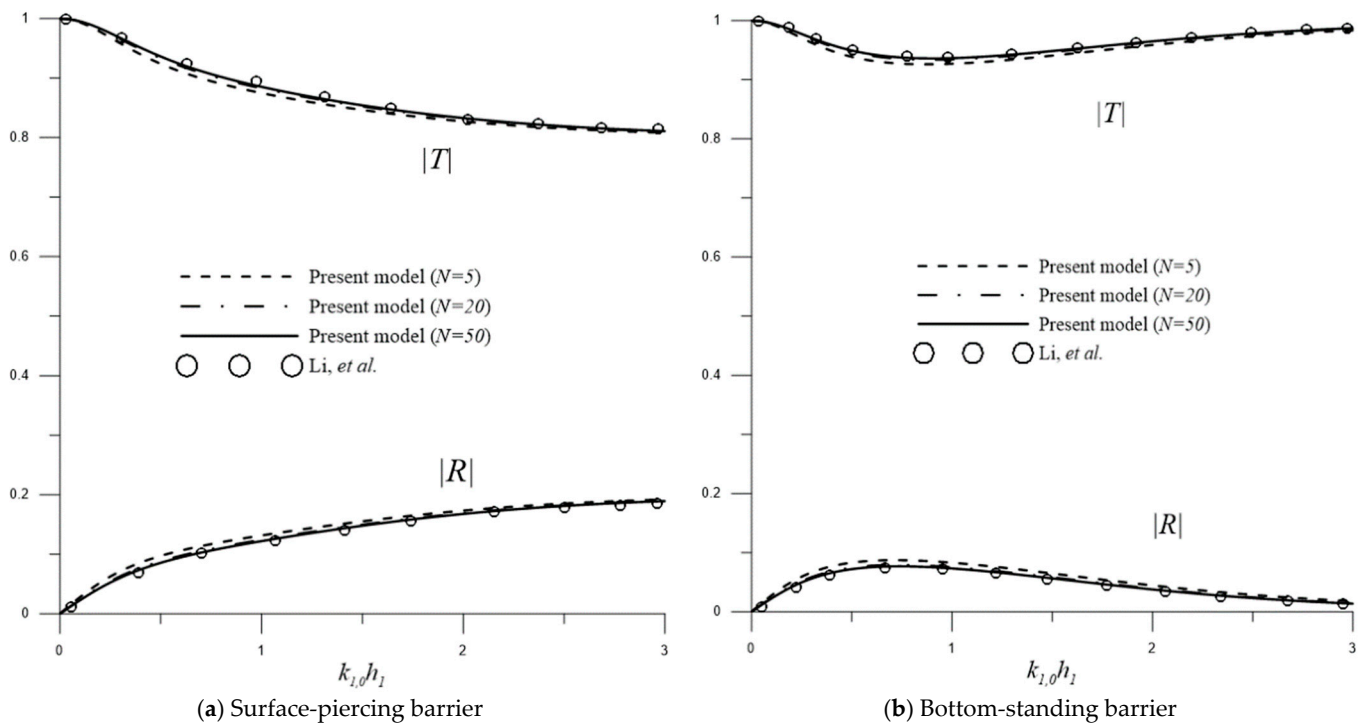
(**b**) Bottom-standing barrier

Figure 3. $|R|$ and $|T|$ with respect to $k_{1,0}h_1$ for a single permeable (**a**) surface-piercing and (**b**) bottom-standing barrier over a flat bottom with different values of G.

EMM was also employed to study the effect of the evanescent mode number N. For the case of a single surface-piercing barrier, the permeability parameter was set to $G = 2$. For the case of a single bottom-standing barrier, the permeability parameter was set to $G = 0.5$.

Figure 4 shows the variations in wave reflection $|R|$ and transmission $|T|$ coefficients as a function of the dimensionless wavenumber $k_{1,0}h_1$ for the cases of an individual permeable surface-piercing and bottom-standing barrier with different values of N. It can be observed from the figure that the curves of $|R|$ and $|T|$ are more similar, corresponding to the literature [10]. The convergence can be observed to be significant, as the results are visually indistinguishable at $N = 50$.

(a) Surface-piercing barrier **(b)** Bottom-standing barrier

Figure 4. $|R|$ and $|T|$ with respect to $k_{1,0}h_1$ for a single permeable (**a**) surface piercing and (**b**) bottom-standing barrier over the flat bottom with different values of N.

Subsequently, the proposed EMM was validated for different incident angles. In addition, the number of evanescent modes was set to $N = 50$ in conjunction with the lengths of the surface-piercing and bottom-standing barriers, which were set to $a/h_1 = 0.5$ and $b/h_1 = 0.5$, respectively. Figure 5 shows the variation in the reflection coefficient $|R|$ with respect to the incident angle γ. As shown in the figures, the numerical results are in good agreement with those reported by Sahoo, et al. [43].

Overall, these results validated the applications of the present EMM for the normal or oblique scattering of water waves by a single thin barrier over a flat bottom, which also counts for permeability.

3.2. Water Wave Scattering by Dual Permeable Barriers over Uniform Bottom

Following Gupta and Gayen [11], the proposed EMM was utilized to estimate the scattering of water waves by dual permeable barriers over a uniform bottom where $h_1 = h_2 = h_3 = 1.0$ m. First, for the case of dual surface-piercing barriers, the permeable parameter was equal to 0.5 and the barrier lengths were set to $a_1/h_1 = 0.4$ and $a_2/h_1 = 0.5$ located at $v_1/h_1 = 0$ and $v_2/h_1 = 0.4$, respectively. For the case of dual bottom-standing barriers, the permeability parameter was set to 1.0, and the barrier lengths were $b_1/h_1 = 0.7$ and $b_2/h_1 = 0.6$ located at $w_1/h_1 = 0$ and $w_2/h_1 = 0.4$, respectively. In addition, the numbers of evanescent modes were set to $N = 50$ and $N = 100$ for dual surface-piercing and bottom-standing barriers, respectively.
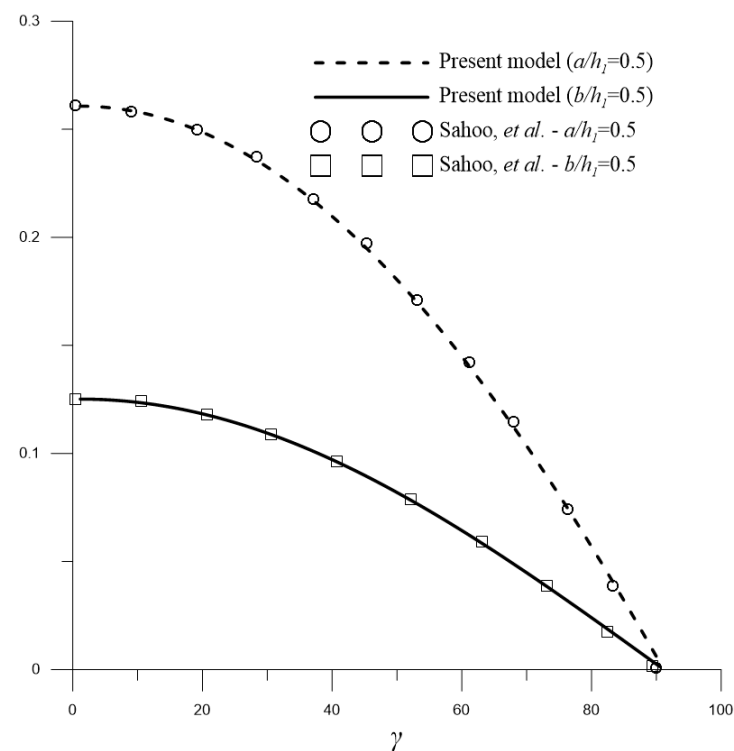
Figure 5. Varying $|R|$ with respect to incidence γ for a single permeable surface-piercing and bottom-standing barrier over the flat bottom.

Figure 6a,b shows the variations in the reflection coefficients with respect to the dimensionless wavenumber $k_{1,0}h_1$ with different values of incidence angles γ for the two circumstances. The results of this figure are in good agreement with the analyses in the literature.
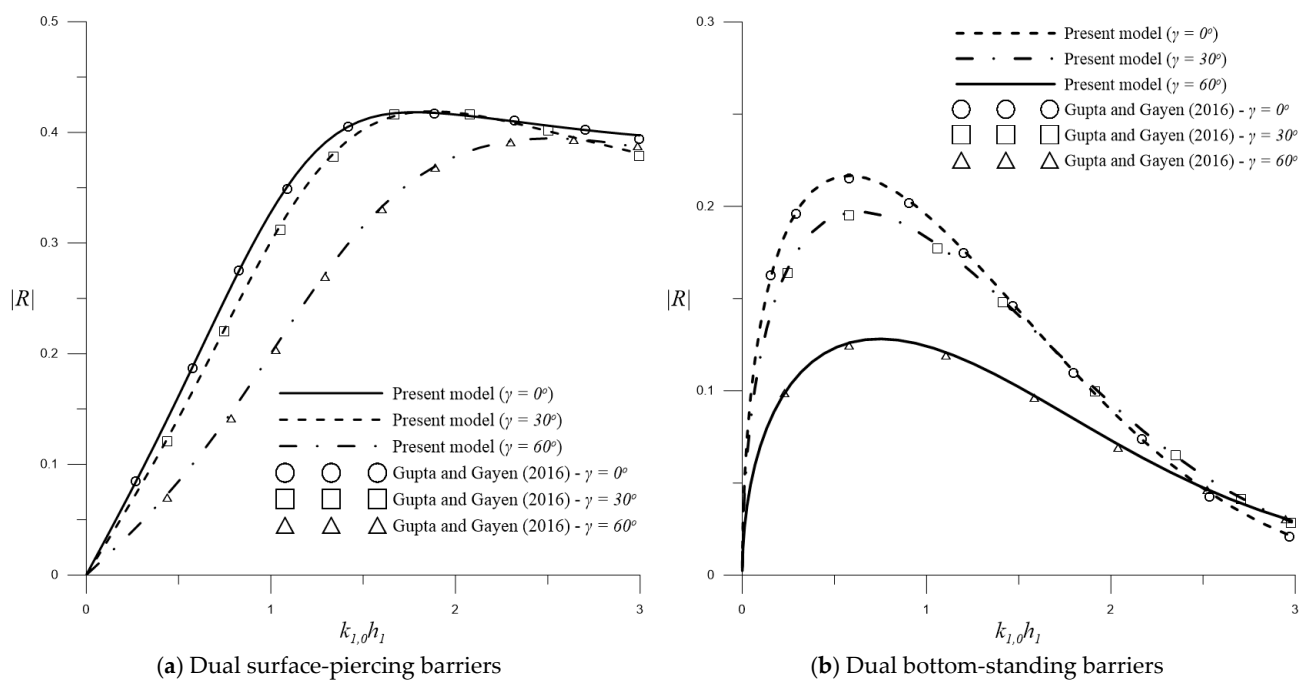

(**a**) Dual surface-piercing barriers

(**b**) Dual bottom-standing barriers

Figure 6. $|R|$ varying incidence γ for dual permeable (**a**) surface-piercing and (**b**) bottom-standing barriers over the flat bottom.

Sequentially, the effect of the evanescent mode number N was additionally examined. Figure 7a,b illustrates the variation in the reflection coefficients $|R|$ with respect to the dimensionless wavenumber $k_{1,0}h_1$ for various values of the permeable parameter G. The barrier lengths and locations were the same as in the previous cases, and $\gamma = 0°$. The values of the permeable parameters G were assumed to be equal to 0.5, 1.0, and $1+\mathbf{i}$. The numerical results were in good agreement with those of Gupta and Gayen [11]. In addition, it was observed that the reflections decrease corresponding to the cases of 0.5, 1.0, and $1+\mathbf{i}$.

(**a**) Dual surface-piercing barriers   (**b**) Dual bottom-standing barriers
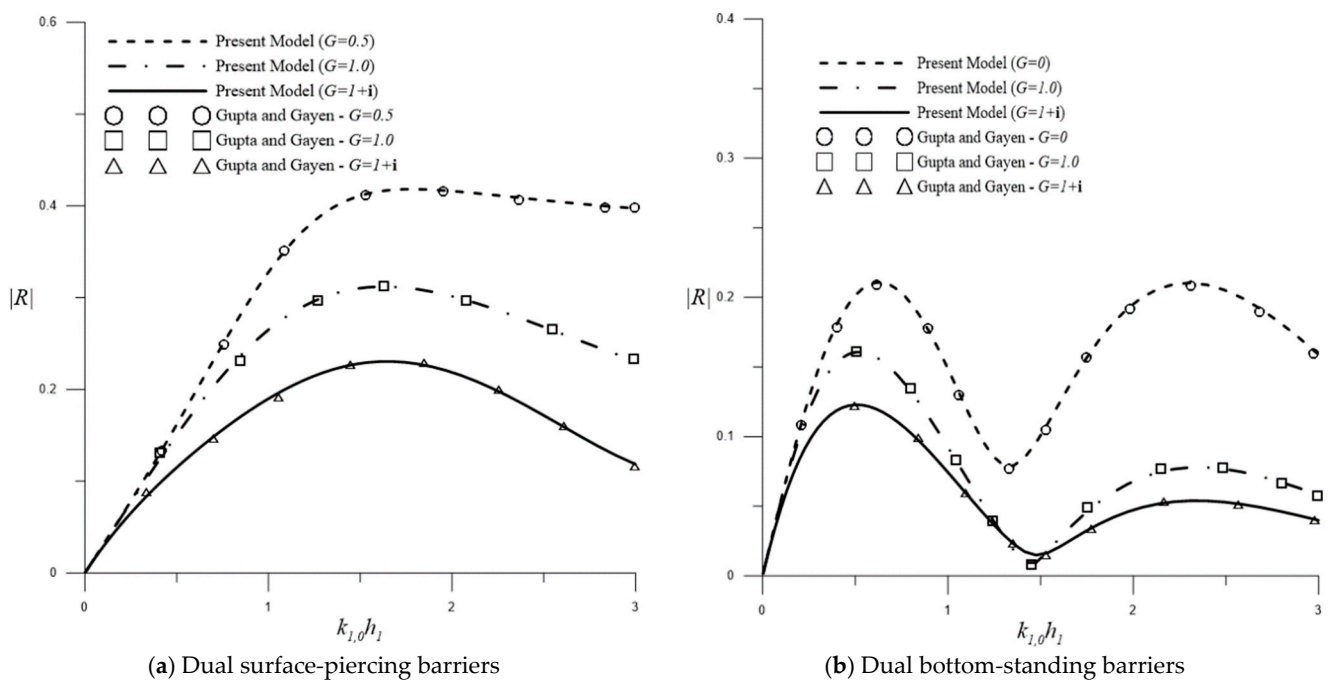
Figure 7. Varying $|R|$ with respect to $k_{1,0}h_1$ for dual permeable (**a**) surface-piercing and (**b**) bottom-standing barriers over the flat bottom with different values of permeable parameters G.

From these results, the proposed EMM has been validated for solving problems of normal or oblique water wave diffraction by multiple permeable barriers with complex-valued permeable parameters over a uniform bottom.

3.3. Water Wave Scattering over Periodic Breakwaters

To substantiate the application of EMM against variable bottoms, we studied wave scattering by a series of periodic trapezoidal or half-cosine breakwaters. The definitions of these breakwaters are presented in Figure 8.
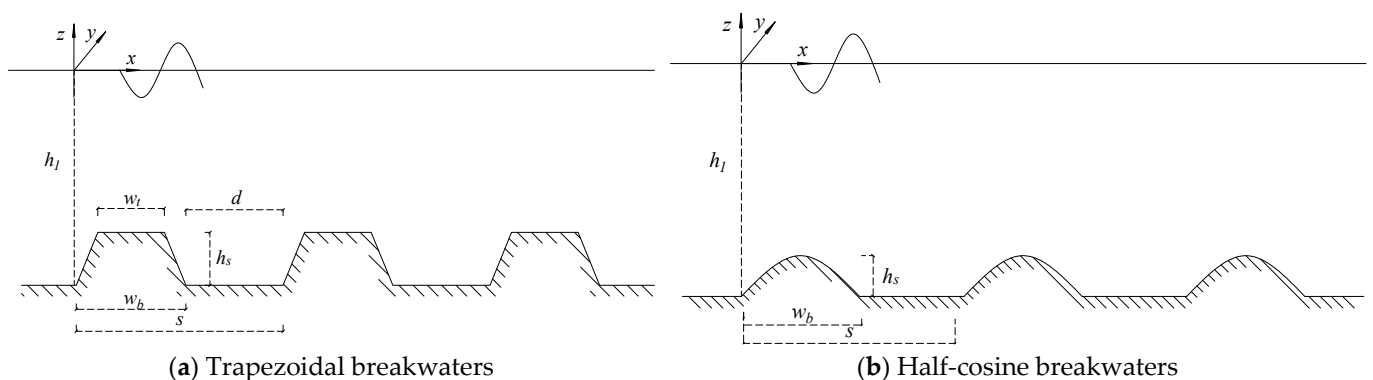

(**a**) Trapezoidal breakwaters   (**b**) Half-cosine breakwaters

Figure 8. Two types of periodic breakwaters: (**a**) trapezoidal breakwater; (**b**) half-cosine breakwater.

Following Cho, et al. [44], we investigated the scattered water wave by J trapezoidal breakwaters. Parameters of the problem were set as $h_1 = 1.0$ m, $h_s = 0.5h_1$, $w_b = h_1$, $w_t = 0.5h_1$, and $s = 2\pi/K = 2h_1$, as shown in Figure 8a. Following Tsai, et al. [45], the numbers of shelves and evanescent modes were set to $M = 100$ and $N = 4$, respectively. Figure 9a depicts the variation of reflection coefficients $|R|$ against $2k_{1,0}/K$ with the number of breakwaters J equal to 1, 2, and 3, respectively. As expected, the computed results were in good agreement with the literature [44]. In addition, the Bragg resonance could be observed to be significant with $2k_{1,0}/K = 1$ for the cases of $J = 2$ and $J = 3$.
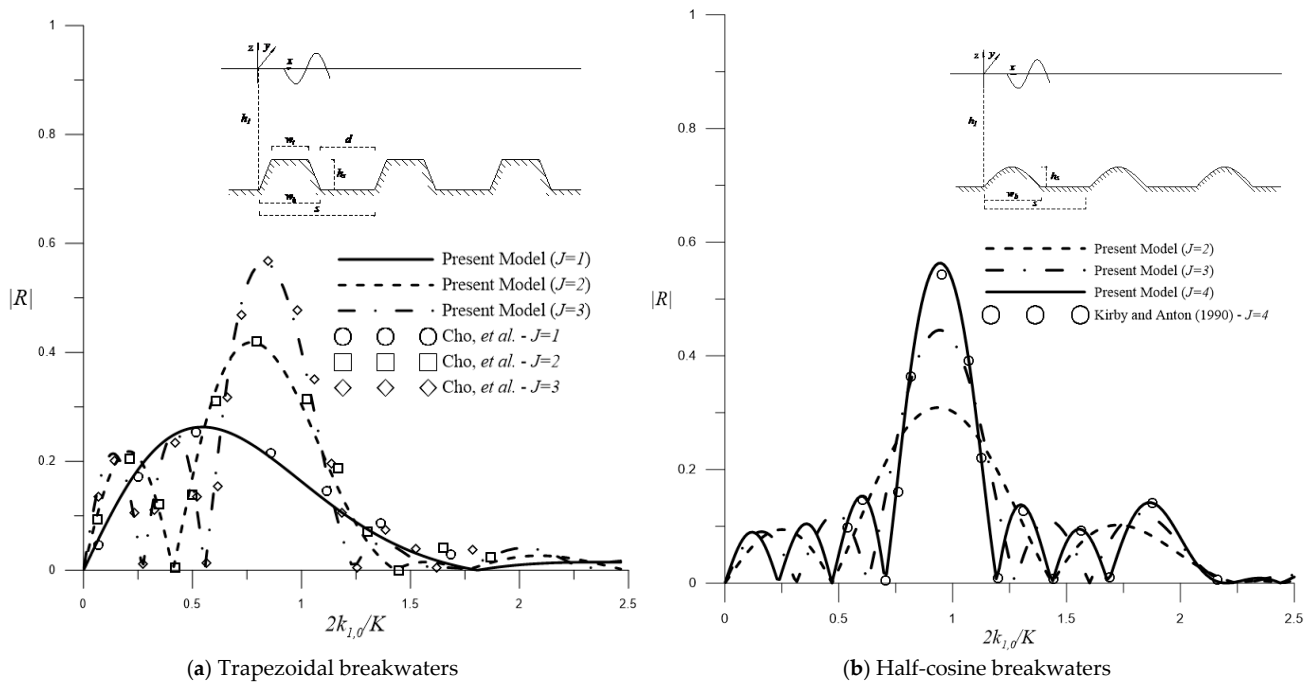

(**a**) Trapezoidal breakwaters

(**b**) Half-cosine breakwaters

Figure 9. Varying $|R|$ with respect to dimensionless $2k_{1,0}/K$ of the (**a**) trapezoidal shape and (**b**) half-cosine bottom for different numbers of J.

Sequentially, the issue of scattered water waves by J half-cosine breakwaters was considered. The bottom profile of the breakwaters is given by:

$$h(x) = h_1 + h_s \cos \frac{\pi}{w_b}[x - (j-1)\lambda], \ (j-1)s - \frac{w_b}{2} \le x \le (j-1)s + \frac{w_b}{2}, \text{with } j = 1, 2, \dots, J, \quad (38)$$

where the parameters were set to $h_1 = 0.15$ m, $s = 2\pi/K = 0.8$ m, $w_b = 0.5$ m, and $h_s = 0.05$ m, as shown in Figure 8b. The number of shelves and evanescent modes were set to be the same as those in the previous cases. The numerical results are presented in Figure 9b. In the figure, the variations in the reflection coefficients $|R|$ are given against the dimensionless parameters $2k_{1,0}/K$ with J equal to 2, 3, and 4. The results of $J = 4$ were in good agreement with those obtained by Kirby and Anton [46]. In addition, the Bragg resonance was found to be significant with $2k_{1,0}/K = 1$.

3.4. Water Scattering by Fully Submerged Barriers behind an Undulated Bottom

Scattered water waves under the combined effects of permeable barriers and undulation bottoms were investigated. Following Kaligatla, et al. [47], the wave period of the incident wave was arranged as $T = 8\,\text{sec}$, and the permeable parameter was set to $G = (1 + \mathbf{i})k_{1,0}$. Therefore, the jth fully submerged barrier is located at $x = v_j = jv_1$, as shown in Figure 10. In addition, the horizontal length of the undulated bottom was denoted as v. In the application of EMM, the number of shelves was set to $M = 100$, and no evanescent mode was considered, similar to Kaligatla, et al. [47].
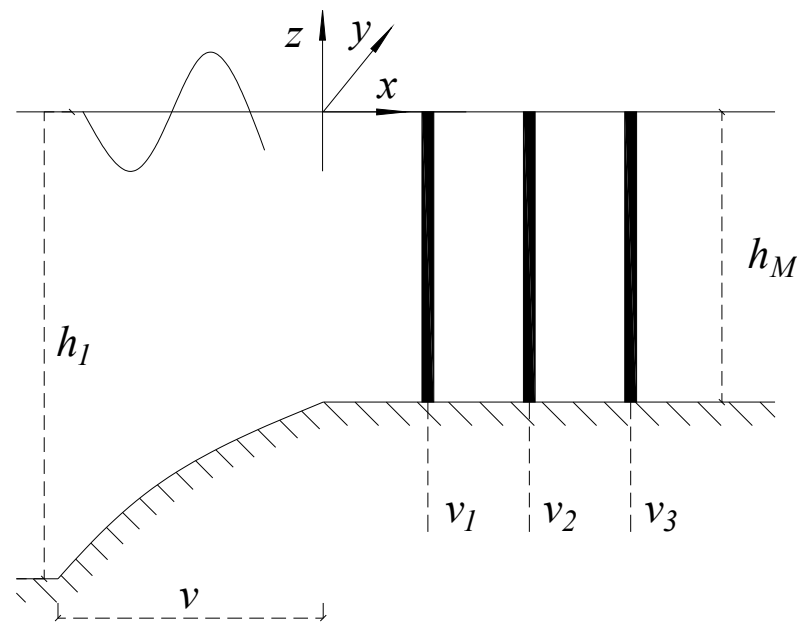
Figure 10. Water waves are scattered by undulation bottom and multiple fully submerged permeable barriers.

Figure 11 shows the variations in the reflection coefficient $|R|$ with respect to v/λ for a different number of permeable thin barriers with water waves with normal approach incidence. It can be observed from the figure that $|R|$ degenerates from medium values for greater relative wave depth $h_M/h_1 = 0.5$ at smaller bottom lengths, and it becomes approximately constant as the length of the bottom increases. These results are in good agreement with those reported in the literature [47].
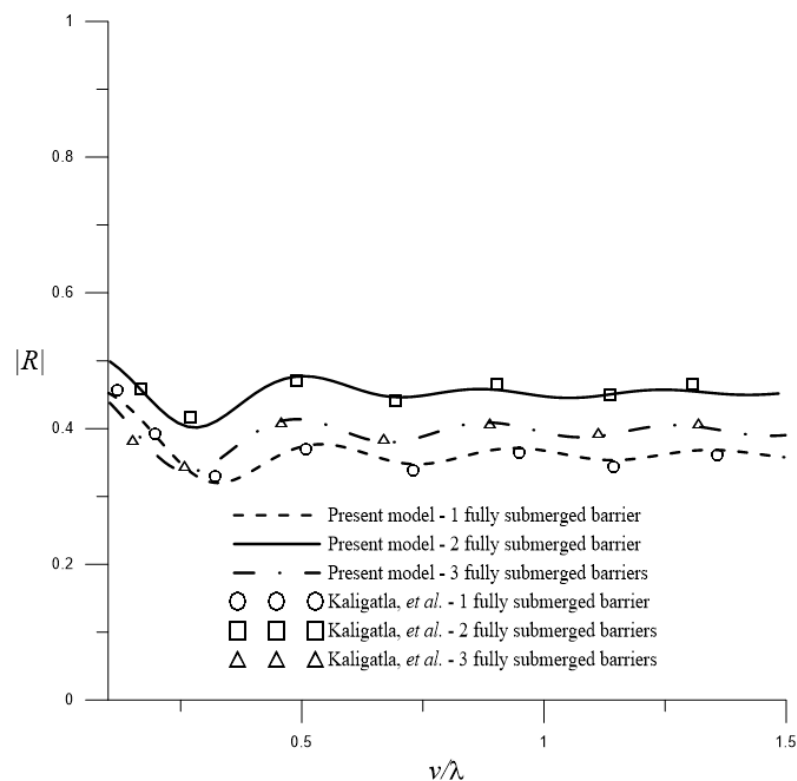
Figure 11. Variations in $|R|$ with respect to v/λ for fully submerged permeable barriers over undulation bottom.

In summary, the results in this subsection imply that the proposed EMM can be implemented to deal with the diffraction of water waves by multiple fully submerged permeable barriers behind an undulated bottom.

4. Discussion

4.1. Permeable Thin Barriers with Trapezoidal Breakwaters

The present EMM model was implemented to analyze the Bragg resonance of water waves by the combined effects of thin permeable barriers and a series of trapezoidal breakwaters. Here, the numbers of shelves, evanescent modes, and trapezoidal breakwaters were set to $M = 100$, $N = 50$, and $J = 3$, respectively.

4.1.1. Bottom-Standing Barriers

Influence of Breakwater Amplitudes

The effect of the breakwater amplitudes was examined by fixing the water depth at $h_1 = 1.0$ m and changing the amplitudes of the trapezoidal breakwater to $h_s/h_1 = 0, 0.1,$ 0.3, and 0.5. The three permeable bottom-standing barriers were located at $w_1 = 0.5w_b$, $w_2 = w_1 + s$, and $w_3 = w_2 + s$, with equal barrier lengths $b_1/h_1 = b_2/h_1 = b_3/h_1 = 0.3$. The permeability parameters of the permeable barriers were set to $G = 0.5$. The other parameters were the same as those in Section 3.3.

The diffractions of water waves, including reflection $|R|$ and transmission $|T|$ coefficients, were calculated against $2k_{1,0}/K$, and the computational results are plotted in Figure 12. The data in the figure indicate that when the amplitudes of the trapezoidal bottom increased, $|R|$ and $|T|$ increased and decreased, respectively. In addition, it can be observed from the figure that the magnitude of the Bragg resonance increased with an increase in the breakwater amplitudes.
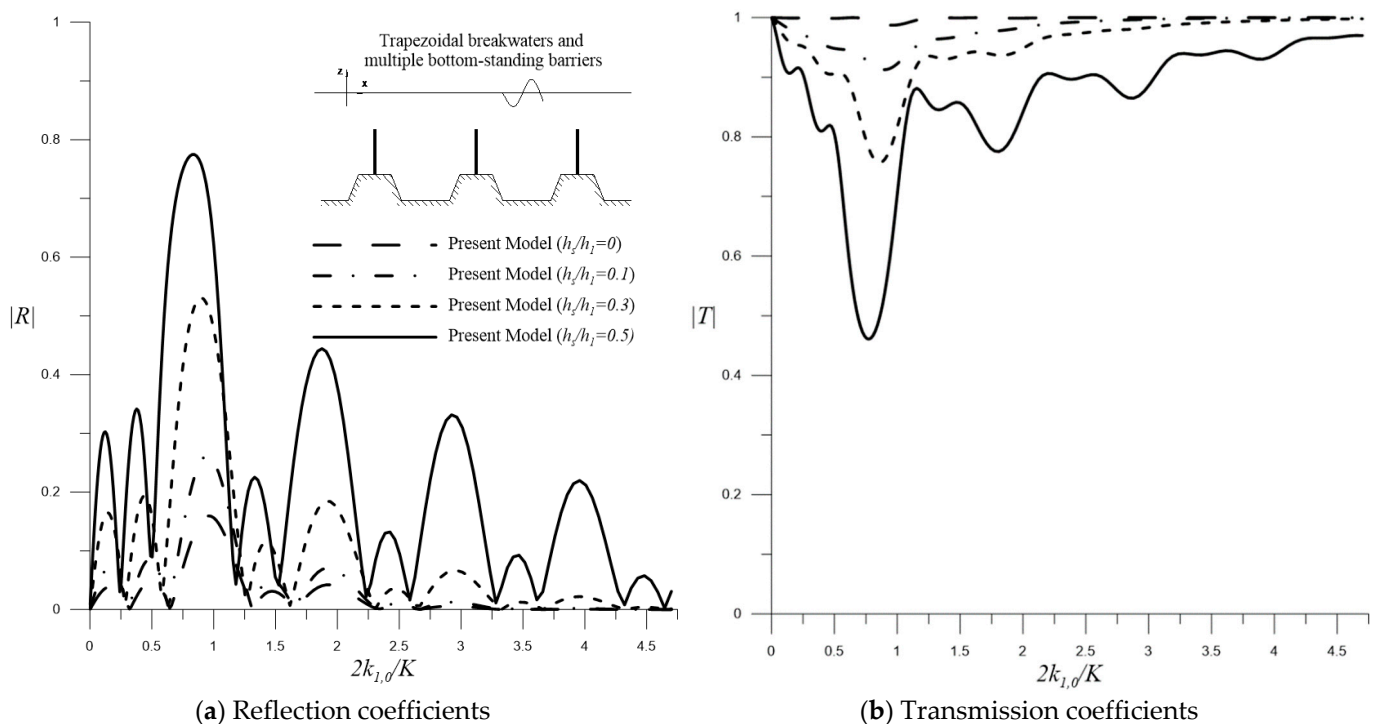

(a) Reflection coefficients

(b) Transmission coefficients

Figure 12. Variations in (**a**) reflection $|R|$ and (**b**) transmission $|T|$ coefficients with respect to $2k_{1,0}/K$ for permeable bottom-standing barriers over trapezoidal breakwaters with different values of h_s/h_1.

Influence of Permeable Parameters

Sequentially, we studied the consequences of the permeable parameters on the Bragg resonance of the water wave by periodic permeable bottom-standing barriers and trape-

zoidal breakwaters. The amplitude of the trapezoidal breakwaters was set to $h_s/h_1 = 0.3$. In addition, different values of permeable parameters are considered: $G + 0$, $G = 0.5$, $G = 1.0$, and $G = 1 + \mathbf{i}$. All other parameters were set the same as those in the previous case.

Before discussing the results, the physical meaning of the permeable parameter G was introduced in accordance with Chwang [48] and Kaligatla, et al. [47]. The real part of the parameter G is associated with the flow resistibility of permeable structures, while the imaginary part is associated with the inertia of the fluid inside the structures. The thin barrier becomes rigid and transparent with $|G| \to 0$ and $|G| \to \infty$, respectively.

The reflection coefficients $|R|$ of the water waves were calculated with respect to the dimensionless parameters $2k_{1,0}/K$, as illustrated in Figure 13. As the permeable parameters $|G|$ increase, the Bragg reflections tend to become weaker. Bragg resonance is expected to disappear when the value of $|G|$ becomes sufficiently large such that the permeable bottom-standing barriers are transparent.
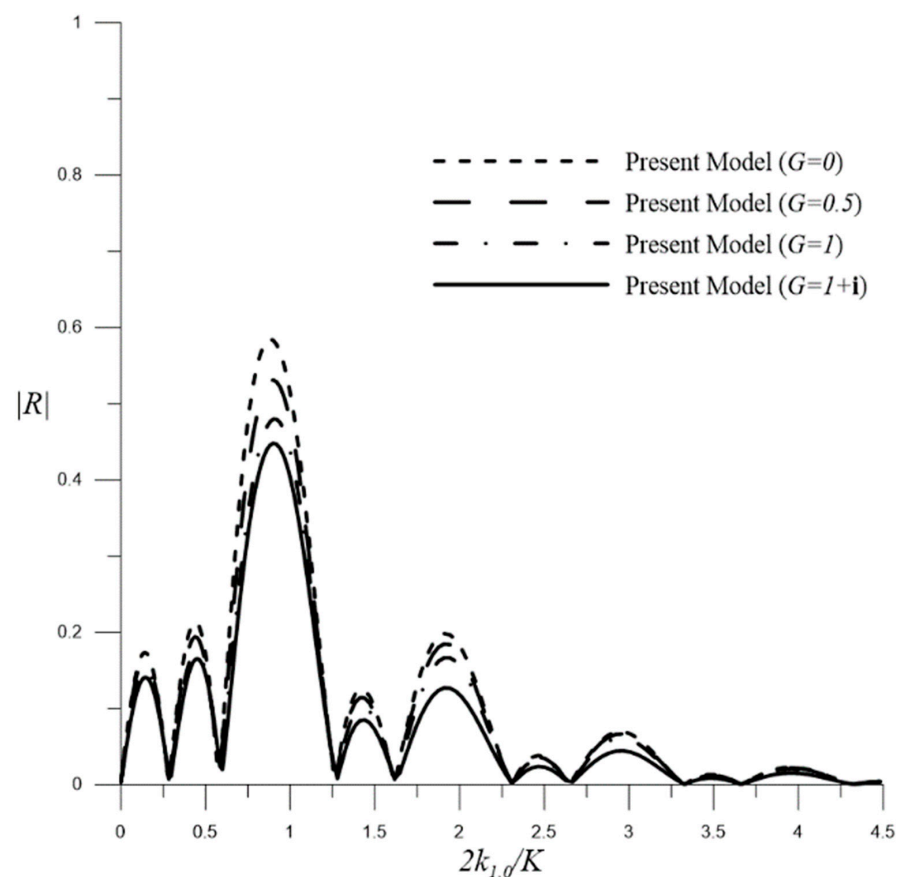

Figure 13. Variations in $|R|$ with respect to $2k_{1,0}/K$ for permeable bottom-standing barriers over trapezoidal breakwaters with different values of G.

4.1.2. Surface-Piercing Barriers

Influence of Breakwater Amplitudes

Subsequently, the amplitudes of water wave scattering by the trapezoidal breakwaters were studied using three pairs of permeable surface-piercing barriers over a breakwater. The water depth was set to $h_1 = 1.0$ m. The breakwater amplitudes had four values: $h_s/h_1 = 0, 0.1, 0.3$, and 0.5. The three permeable surface-piercing barriers were located at $v_1 = 0.5w_b$, $v_2 = v_1 + s$, and $v_3 = v_2 + s$ with equal barrier lengths $a_1/h_1 = a_2/h_1 = a_3/h_1 = 0.1$. The permeability parameter was set to $G = 0.5$.

The reflection $|R|$ and transmission $|T|$ coefficients were studied with respect to different values of h_s/h_1, and the numerical results are plotted in Figure 14. The primary Bragg resonance was found to be significant when the value of $2k_{1,0}/K$ was approximately

1. In addition, the secondary resonance was observed to be $2k_{1,0}/K \to 2$. The increase of breakwater amplitudes enhances the magnitudes of the primary Bragg resonance. However, when the periodic bottom becomes flatter (h_s/h_1 smaller), the reflection coefficient $|R|$ becomes stronger for higher-order resonances. This is because the higher-order Bragg resonance by surface-piercing barriers is more magnified for flatter bottoms since the corresponding wavelengths become shorter, and get concentrated on the free surface.

(**a**) Reflection coefficients

(**b**) Transmission coefficients
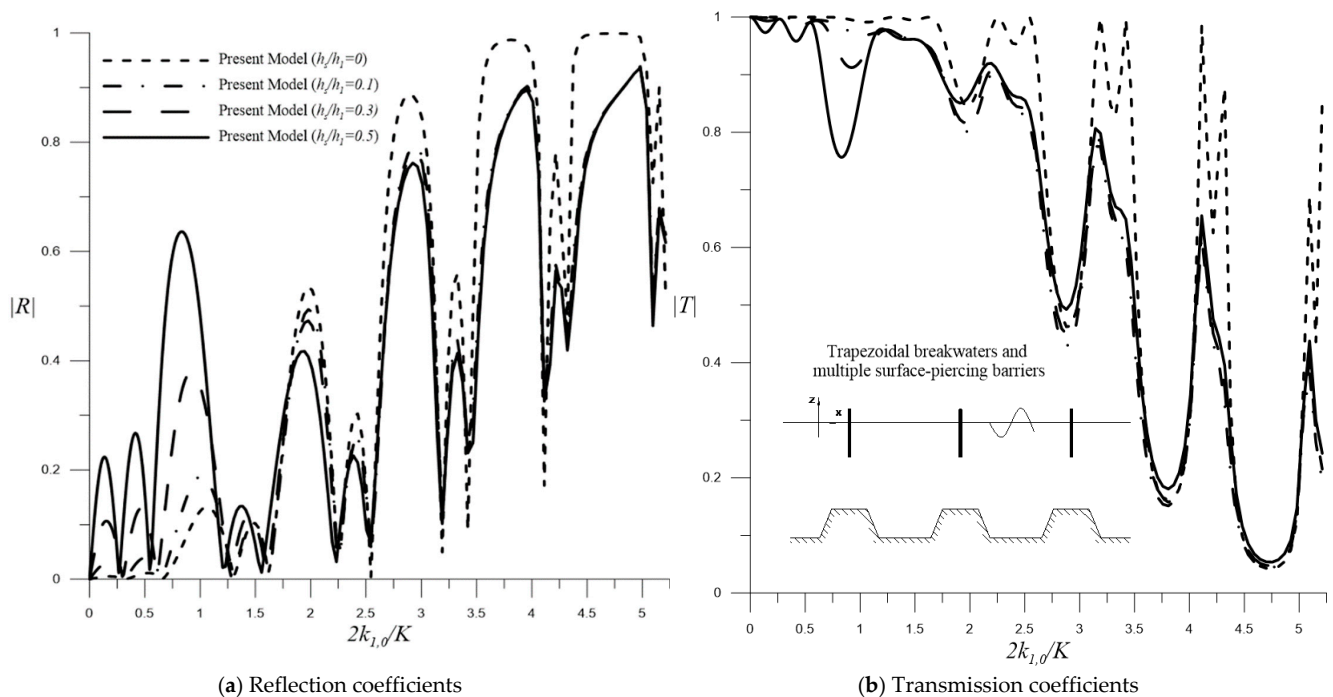
Figure 14. Variations in (**a**) reflection $|R|$ and (**b**) transmission $|T|$ coefficients with respect to $2k_{1,0}/K$ for permeable surface-piercing barriers over trapezoidal breakwaters with different values of h_s/h_1.

Influence of Permeable Parameters

Subsequently, the effect of the permeable parameters on the Bragg resonance of scattered water waves by periodic permeable surface-piercing barriers in the presence of trapezoidal breakwaters was studied. The amplitude of the trapezoidal breakwaters was set to $h_s/h_1 = 0.3$. In addition, different values of permeability parameters were investigated, such as $G = 0$, $G = 0.5$, $G = 1.0$, and $G = 1 + \mathbf{i}$. All other parameters of the trapezoidal breakwaters were set to be exactly similar to those of the previous case.

Figure 15 presents the reflection coefficient $|R|$ with respect to the dimensionless parameter $2k_{1,0}/K$. In the figure, the Bragg reflections significantly decrease as the permeable parameter $|G|$ increases. This result is similar to that of the previous cases with bottom-standing barriers.

4.1.3. Fully Submerged Permeable Barriers

Subsequently, we study the effect of full submergence by replacing the permeable surface-standing barriers of the previous case with fully submerged ones.

Figure 16 presents the reflection coefficient $|R|$ with respect to the dimensionless parameter $2k_{1,0}/K$ with three different values of permeable parameters: $G = 0.5$, $G = 1.0$, and $G = 1 + \mathbf{i}$. In the figure, it can be observed that the reflections become weaker as the permeable parameter $|G|$ increases, and the Bragg resonance is significant when the value of the dimensionless parameter $2k_{1,0}/K$ is approximately an integer. However, when compared with the results in Figure 15, the effect of the fully submerged permeable barriers is to further magnify the reflection even when the dimensionless parameter $2k_{1,0}/K$ is not close to integers, especially for cases with smaller $|G|$.
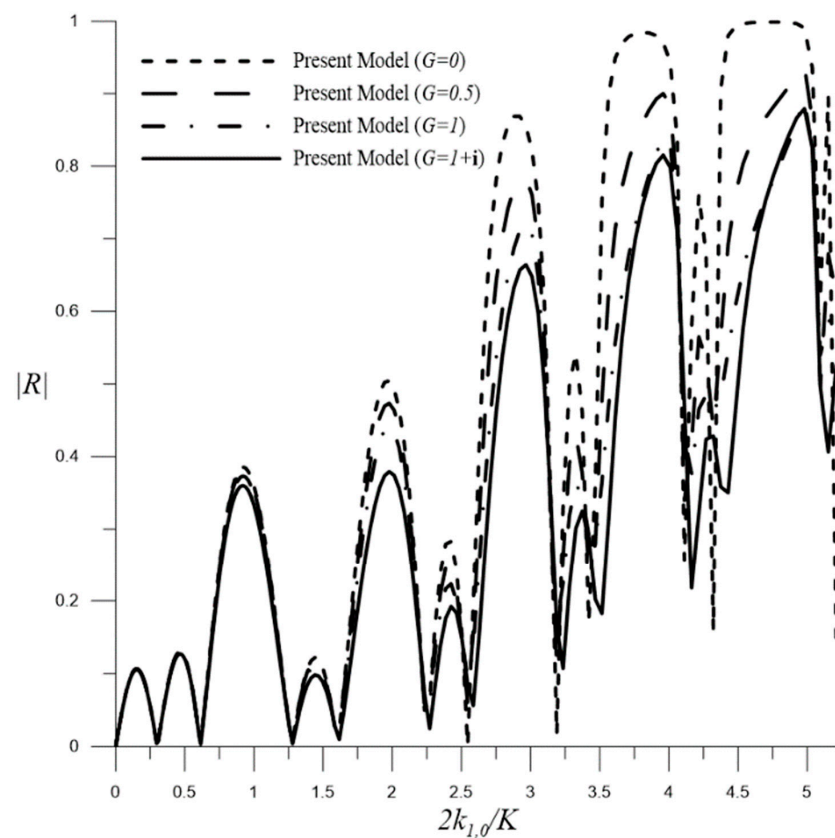
Figure 15. Variations in $|R|$ with respect to $2k_{1,0}/K$ for permeable surface-piercing barriers over trapezoidal breakwaters with different values of G.
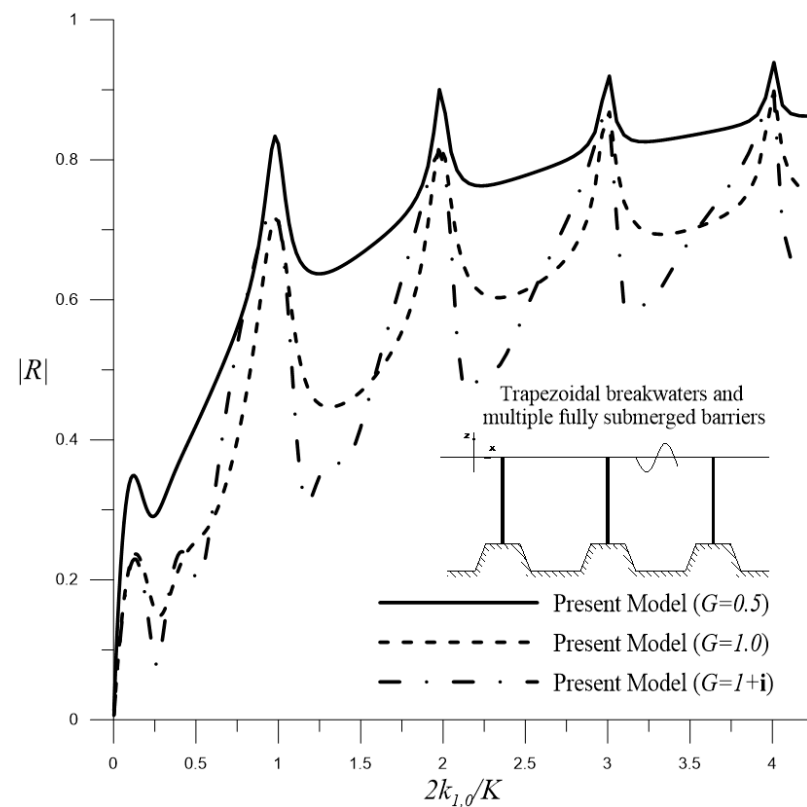

Figure 16. Variations in $|R|$ with respect to $2k_{1,0}/K$ for fully submerged permeable barriers with different values of G.

The effects of the incident angles were subsequently studied using the case shown in Figure 16 with $G = 0.5$. Figure 17 shows the variations in $|R|$ with respect to the dimensionless parameter $2k_{1,0}\cos\gamma/K$ with four incident angle values: $\gamma = 0°, 30°, 45°,$ and $60°$. In the figure, significant Bragg resonance can be observed when the dimensionless parameter $2k_{1,0}\cos\gamma/K$ is approximately an integer. These results validate Bragg's law for oblique incidence.
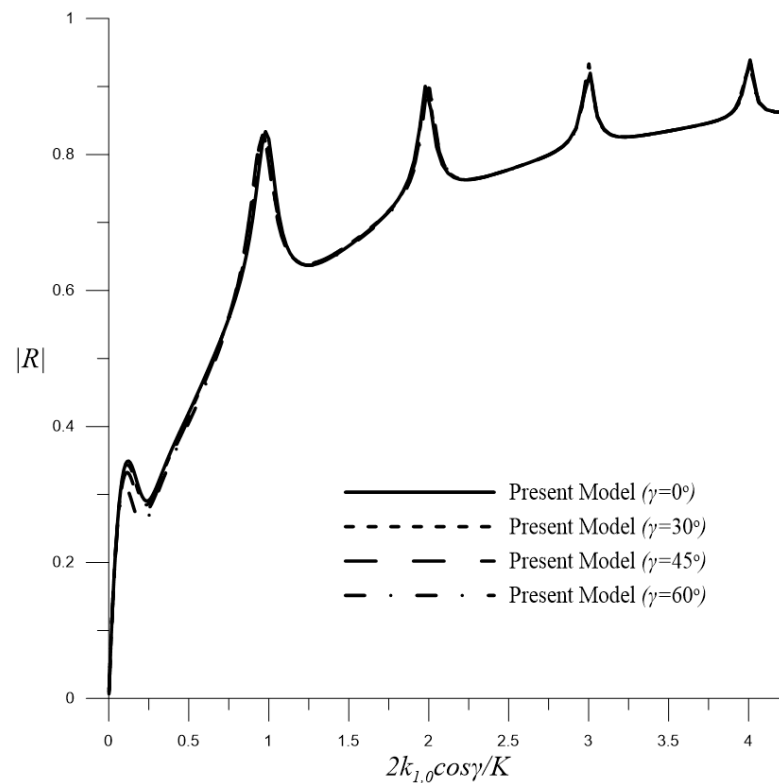

Figure 17. Variations in $|R|$ with respect to $2k_{1,0}\cos\gamma/K$ for fully submerged permeable barriers with different values of γ.

4.2. Permeable Thin Barriers with Half-Cosine Breakwaters

Subsequently, the effects of bottom-standing, surface-piecing, and fully submerged barriers on the periodic breakwaters, demonstrated in Section 4.1, were enforced by considering an array of four half-cosine breakwaters ($J = 4$).

4.2.1. Bottom-Standing Barriers
Influence of Breakwater Amplitudes

In this case, there were four bottom-standing barriers: $w_1 = 0.5w_b$, $w_2 = w_1 + s$, $w_3 = w_2 + s$, and $w_4 = w_3 + s$. The water depth was set to $h_1 = 0.15\ m$. Therefore, the barrier heights and permeable parameters of the four barriers were set to $b_1/h_1 = b_2/h_1 = b_3/h_1 = b_4/h_1 = 0.333$ and $G = 0.5$, respectively. The other parameters were set similarly to those in Figure 9b in Section 3.3.

As demonstrated in Figure 18, the variations in $|R|$ and $|T|$ with respect to $2k_{1,0}/K$ were examined for different values of the breakwater amplitudes: $h_s/h_1 = 0, 0.1, 0.2,$ and 0.3. In the figure, it can be observed that when the amplitudes of the half-cosine bottom increased, the reflection $|R|$ and transmission $|T|$ coefficients increased and decreased, respectively. In addition, the Bragg resonance was significant when the dimensionless parameter $2k_{1,0}/K$ was close to integers, and it increased with the increase in breakwater amplitudes. These results were similar to those shown in Figure 12.
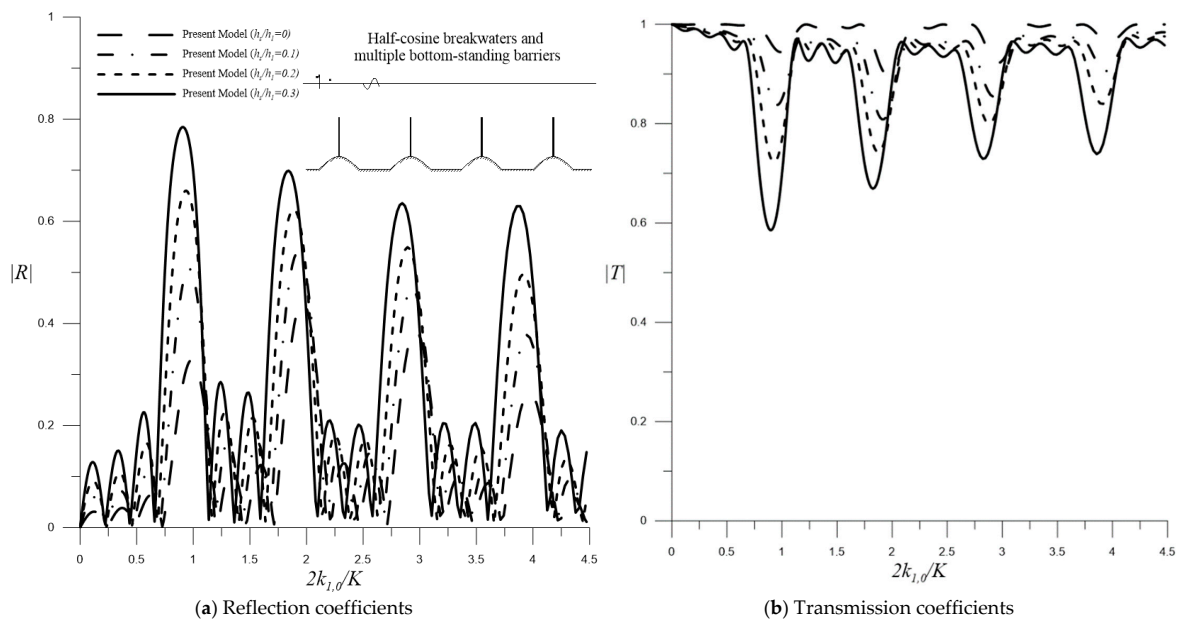
Figure 18. Variations in (**a**) reflection $|R|$ and (**b**) transmisstion $|T|$ coefficient with respect to $2k_{1,0}/K$ for permeable bottom-standing barriers over half-cosine breakwaters with different values of h_s/h_1.

Influence of Permeable Parameters

The effect of the permeable parameters was investigated in the previous case using $h_s/h_1 = 0.2$ with $h_1 = 0.15$ m. Four values of permeable parameters were used: $G = 0$, $G = 0.5$, $G = 1.0$, and $G = 1 + \mathbf{i}$. All other parameters of the half-cosine breakwaters were set to be exactly those of the previous section.

As illustrated in Figure 19, $|R|$ was plotted against the dimensionless parameter $2k_{1,0}/K$. It can be observed from the figure that when the permeable parameter $|G|$ increases, the reflection coefficient $|R|$ decreases slightly, and the Bragg reflections become weaker. These results were similar to those shown in Figure 13.
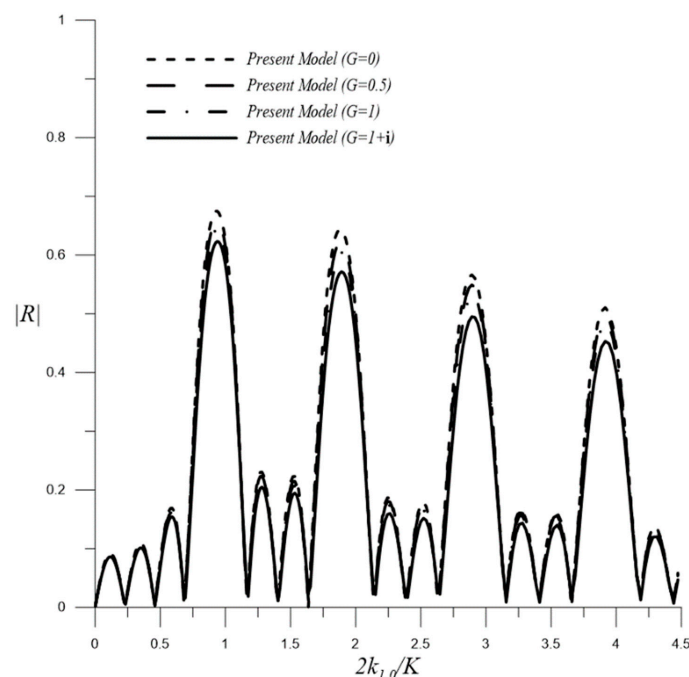

Figure 19. Variations in $|R|$ with respect to $2k_{1,0}/K$ for permeable bottom-standing barriers over half-cosine breakwaters with different values of G.

4.2.2. Surface-Piercing Barriers

Influence of Breakwater Amplitudes

In this case, four surface-piercing barriers were located at $v_1 = 0.5w_b$, $v_2 = v_1 + s$, $v_3 = v_2 + s$, and $v_4 = v_3 + s$, sequentially. In addition, the values of the barrier heights and permeable parameters were configured as $a_1/h_1 = a_2/h_1 = a_3/h_1 = a_4/h_1 = 0.2$ and $G = 0.5$. The breakwater amplitudes had four values: $h_s/h_1 = 0$, 0.1, 0.2, and 0.3.

$|R|$ and $|T|$ were calculated with different values of the dimensionless parameter $2k_{1,0}/K$, and the numerical results are presented in Figure 20. The Bragg resonance was found to be significant when the values of $2k_{1,0}/K$ were close to integers. The increase in breakwater amplitudes increases the magnitudes of the primary Bragg resonance. However, when the periodic bottom becomes flatter (h_s/h_1 smaller), the reflection coefficient $|R|$ becomes stronger for higher-order resonances. These results are similar to those obtained in Figure 14.
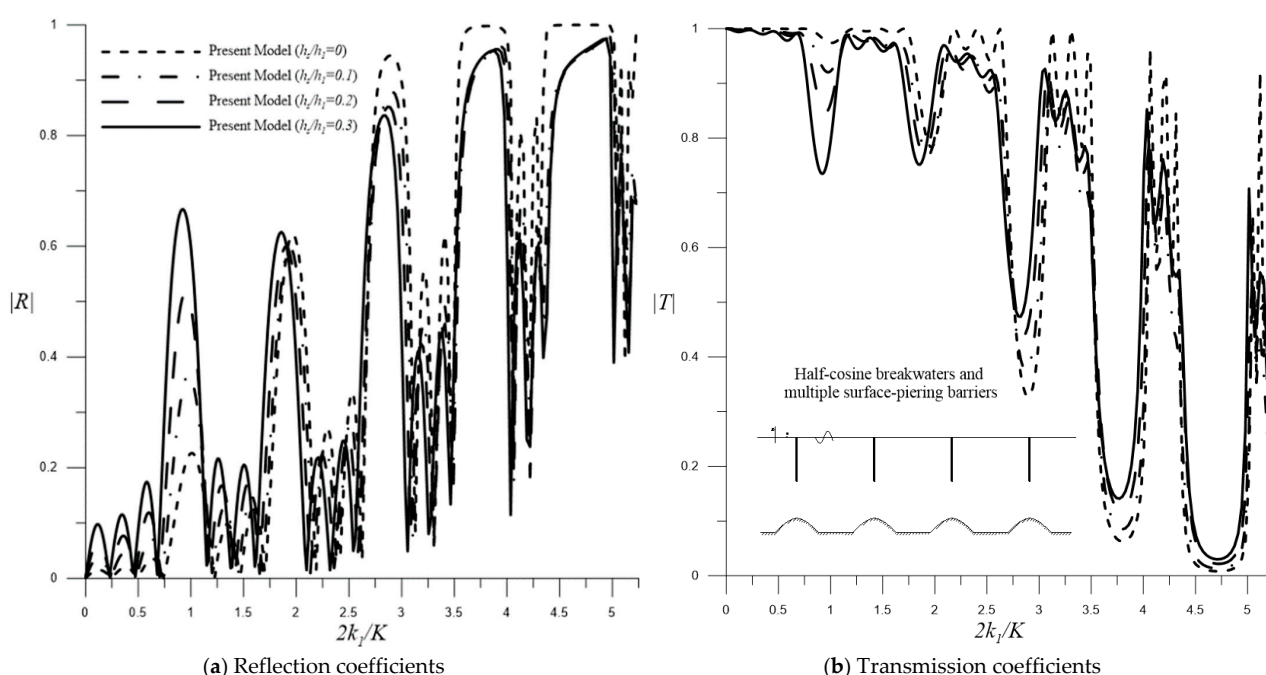

(**a**) Reflection coefficients

(**b**) Transmission coefficients

Figure 20. Variations in (**a**) reflection $|R|$ and (**b**) transmision $|T|$ coefficient with respect to $2k_{1,0}/K$ in the permeable surface-piercing barriers over half-cosine breakwaters with different values of h_s/h_1.

Influence of Permeable Parameters

Subsequently, the present EMM was applied to study the effect of permeable parameters on the Bragg resonance by multiple permeable surface-piercing barriers over half-cosine breakwaters. The amplitude of the half-cosine breakwaters was set to $h_s/h_1 = 0.2$. In addition, different values of permeability parameters were investigated, such as $G = 0$, $G = 0.5$, $G = 1.0$, and $G = 1 + \mathbf{i}$. All other parameters of the half-cosine breakwaters were set to be the same as those of the previous section.

Figure 21 presents the reflection coefficient $|R|$ with respect to the dimensionless parameter $2k_{1,0}/K$. In the figure, the Bragg reflections decrease slightly as the permeable parameter $|G|$ increases. Similar results have been previously reported.

4.2.3. Fully Submerged Permeable Barriers

The permeable surface-standing barriers were replaced in the previous case with fully submerged ones. Figure 22 presents the reflection coefficient $|R|$ with respect to the dimensionless parameter $2k_{1,0}/K$ with three different values of permeable parameters: $G = 0.5$, $G = 1.0$, and $G = 1 + \mathbf{i}$. It can be observed from the figure that the reflections become weaker as the permeable parameter $|G|$ increases, and the Bragg resonance is

obvious when the dimensionless parameter $2k_{1,0}/K$ is approximately an integer. However, compared with the results obtained in Figure 21, the effect of the fully submerged permeable barriers is to further strengthen the reflection, especially for cases with more minor $|G|$.
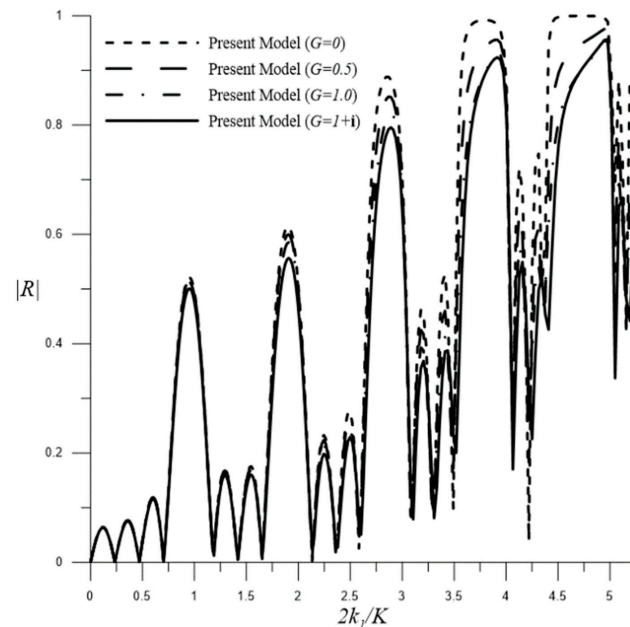

Figure 21. Variations in $|R|$ with respect to $2k_{1,0}/K$ for permeable surface-piercing barriers over half-cosine breakwaters with different values of G.
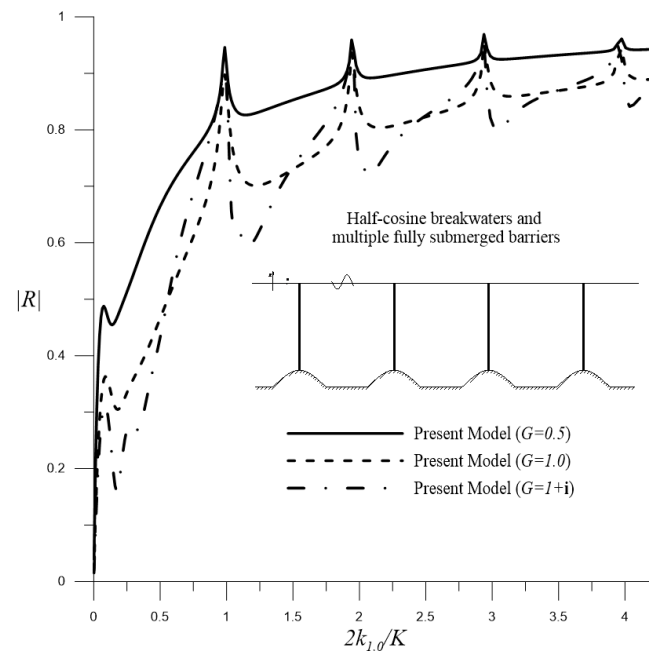

Figure 22. Variations in $|R|$ with respect to $2k_{1,0}/K$ for fully submerged permeable barriers over half-cosine breakwaters with different values of G.

The effects of the incident angles were sequentially studied using the case shown in Figure 22 with $G = 0.5$. Figure 23 presents the computational results of the reflection coefficient $|R|$ with respect to the dimensionless parameter $2k_{1,0} \cos \gamma /K$ with four values of incident angles: $\gamma = 0°$, $30°$, $45°$, and $60°$. In the figure, significant Bragg resonance can be observed when the dimensionless parameter $2k_{1,0} \cos \gamma /K$ is close to integers.
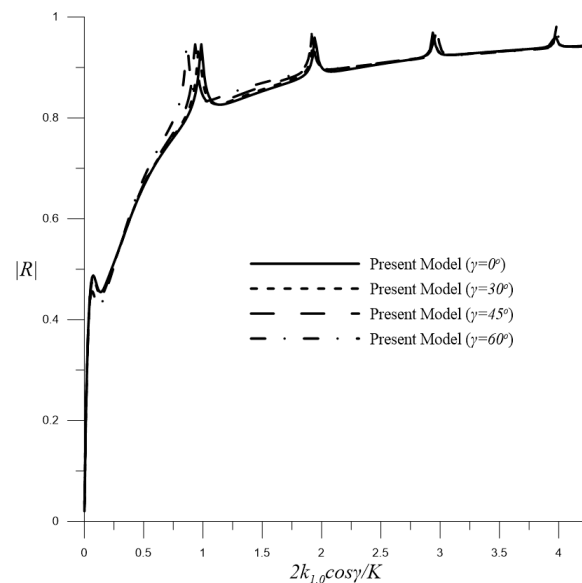
Figure 23. Variations in $|R|$ with respect to $2k_{1,0} \cos \gamma / K$ for fully submerged permeable barriers over half-cosine breakwaters with different values of incident angles γ.

4.3. Energy Loss

In the present investigation, energy dissipation was introduced by permeable thin barriers. The water wave energy loss coefficient E_{loss} is formulated as follows:

$$E_{loss} = 1 - \left(|R|_2 + |T|^2 \right), \tag{39}$$

where equal upstream and downstream water depths were assumed.

Figure 24a,b illustrate the variation in energy loss E_{loss} against dimensionless $2k_{1,0}/K$ with different values of the permeable parameter G for Bragg scattering of water waves by multiple periodic fully submerged permeable barriers over periodic trapezoidal and half-cosine breakwaters, for which the configurations are exactly the same as those in Figures 16 and 22, respectively. As demonstrated in the figure, it is obvious that the energy losses are smaller for cases with smaller permeable parameters $|G|$ or shorter wavelengths. In addition, the energy losses are minimized when Bragg resonance occurs.
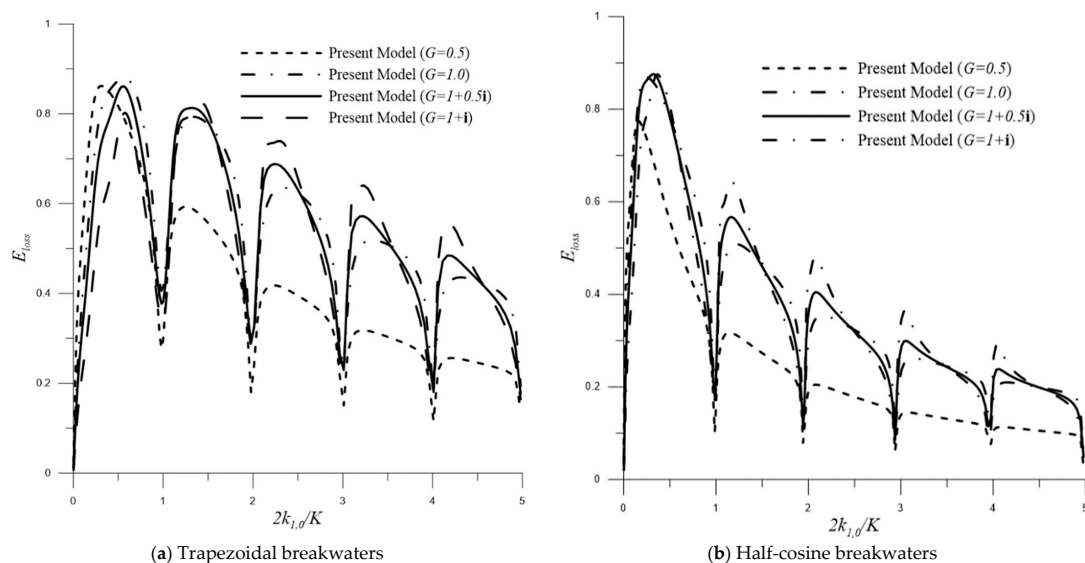

(**a**) Trapezoidal breakwaters   (**b**) Half-cosine breakwaters

Figure 24. Variations in E_{loss} with respect to dimensionless parameter $2k_{1,0}/K$ over (**a**) trapezoidal breakwaters and (**b**) half-cosine breakwaters with different values of G.

5. Conclusions

In this study, an EMM solution was developed to investigate the Bragg resonance of water waves by multiple thin permeable barriers owing to periodic breakwaters. The bottom topography was discretized into multiple shelves and sequentially determined. The proposed method consisted of eigenfunctions, and was solved using the conservations of mass and momentum. The SuperLU sparse matrix solver was applied to solve the resulting system of linear equations. The proposed method degenerates to traditional EMM formulations if thin barriers, barrier permeability, or bottom undulations are not considered. Sequentially, the EMM was validated by the diffraction of surface water waves by three types of permeable barriers: surface-piercing, bottom-standing, and fully submerged barriers. Furthermore, the effects of periodic breakwaters on the Bragg resonance were discussed. Finally, EMM was applied to study the impact of multiple barriers on Bragg resonance by a series of periodic trapezoidal or half-cosine breakwaters. In the cases of multiple bottom-standing barriers, the magnitude of the Bragg resonance increases with an increase in the breakwater amplitude. However, for surface-piecing barriers, when the periodic bottom becomes flatter, the reflection coefficient becomes stronger for higher-order resonances because the motions of shorter waves are concentrated near the free surface. Overall, barriers with higher permeability parameters exhibited weaker water wave reflections. In the case of fully submerged barriers, the reflection effects become even more significant. In addition, loss of wave energy was observed with different values of the barrier permeability parameter. As the permeability parameters decreased, the wave energy dissipated less. The energy losses were the least when Bragg resonance occurred.

Author Contributions: Conceptualization, C.-T.T., C.L. and C.-C.T.; methodology, C.-T.T. and C.-C.T.; visualization C.-T.T. and C.-C.T.; writing—original draft, C.-T.T. and C.-C.T.; supervision, C.L. and C.-C.T. All authors have read and agreed to the published version of the manuscript.

Data Availability Statement: The data will be provided on request to the corresponding author.

Conflicts of Interest: The authors declare no conflict of interest.

References

1. Porter, R.; Evans, D.V. Complementary approximations to wave scattering by vertical barriers. *J. Fluid Mech.* **1995**, *294*, 155–180. [CrossRef]
2. Losada, I.J.; Losada, M.A.; Roldán, A. Propagation of oblique incident waves past rigid vertical thin barriers. *Appl. Ocean Res.* **1992**, *14*, 191–199. [CrossRef]
3. Losada, M.A.; Losada, I.J.; Roldán, A.J. Propagation of oblique incident modulated waves past rigid, vertical thin barriers. *Appl. Ocean Res.* **1993**, *15*, 305–310. [CrossRef]
4. Losada, I.J.; Losada, M.A.; Losada, R. Wave spectrum scattering by vertical thin barriers. *Appl. Ocean Res.* **1994**, *16*, 123–128. [CrossRef]
5. Abul-Azm, A.G. Wave diffraction through submerged flexible breakwaters. *Ocean Eng.* **1996**, *23*, 403–422. [CrossRef]
6. Ursell, F. The effect of a fixed vertical barrier on surface waves in deep water. *Math. Proc. Camb. Philos. Soc.* **1947**, *43*, 374–382. [CrossRef]
7. Das, P.; Dolai, D.P.; Mandal, B.N. Oblique Wave Diffraction by Parallel Thin Vertical Barriers with Gaps. *J. Waterw.* **1997**, *123*, 163–171. [CrossRef]
8. Dalrymple, R.A.; Losada, M.A.; Martin, P.A. Reflection and transmission from porous structures under oblique wave attack. *J. Fluid Mech.* **1991**, *224*, 625–644. [CrossRef]
9. Lee, M.; Chwang, A.T. Scattering and radiation of water waves by permeable barriers. *Phys. Fluids* **2000**, *12*, 54–65. [CrossRef]
10. Li, A.-J.; Liu, Y.; Li, H.-J. Accurate solutions to water wave scattering by vertical thin porous barriers. *Math. Probl. Eng.* **2015**, *3*, 985731. [CrossRef]
11. Gupta, S.; Gayen, R. Scattering of oblique water waves by two thin unequal barriers with non-uniform permeability. *J. Eng. Math.* **2018**, *112*, 37–61. [CrossRef]
12. Macaskill, C. Reflexion of water waves by a permeable barrier. *J. Fluid Mech.* **1979**, *95*, 141–157. [CrossRef]
13. Takano, K. Effets d'un obstacle parallelepipedique sur la propagation de la houle. *La Houille Blanche* **1960**, *15*, 247–267. [CrossRef]
14. Newman, J.N. Propagation of water waves over an infinite step. *J. Fluid Mech.* **1965**, *23*, 399–415. [CrossRef]

15. Mei, C.C.; Black, J.L. Scattering of surface waves by rectangular obstacles in waters of finite depth. *J. Fluid Mech.* **1969**, *38*, 499–511. [CrossRef]

16. Kirby, J.T.; Dalrymple, R.A. Propagation of obliquely incident water waves over a trench. *J. Fluid Mech.* **1983**, *133*, 47–63. [CrossRef]

17. Kirby, J.T.; Dalrymple, R.A.; Seo, S.N. Propagation of obliquely incident water waves over a trench. Part 2. Currents flowing along the trench. *J. Fluid Mech.* **1987**, *176*, 95–116. [CrossRef]

18. Devillard, P.; Dunlop, F.; Souillard, B. Localization of gravity waves on a channel with a random bottom. *J. Fluid Mech.* **1988**, *186*, 521–538. [CrossRef]

19. O'Hare, T.J.; Davies, A. A new model for surface wave propagation over undulating topography. *Coast. Eng.* **1992**, *18*, 251–266. [CrossRef]

20. Tsai, C.-C.; Hsu, T.-W.; Lin, Y.-T. On step approximation for Roseau's analytical solution of water waves. *Math. Probl. Eng.* **2011**, *2011*, 607196. [CrossRef]

21. Tsai, C.-C.; Lin, Y.-T.; Hsu, T.-W. On step approximation of water-wave scattering over steep or undulated slope. *Ocean Eng.* **2014**, *24*, 98–105. [CrossRef]

22. Tsai, C.-C.; Chang, Y.-H.; Hsu, T.-W. Step approximation on oblique water wave scattering and breaking by variable porous breakwaters over uneven bottoms. *Ocean Eng.* **2022**, *253*, 111325. [CrossRef]

23. Isaacson, M.; Premasiri, S.; Yang, G. Wave interactions with vertical slotted barrier. *J. Waterw.* **1998**, *124*, 118–126. [CrossRef]

24. Poguluri, S.K.; Cho, I.H. Analytical and numerical study of wave interaction with a vertical slotted barrier. *Ships Offshore Struct.* **2021**, *16*, 1012–1024. [CrossRef]

25. Tran, C.-T.; Chang, J.-Y.; Tsai, C.-C. Step approximation for water wave scattering by multiple thin barriers over undulated bottoms. *J. Mar. Sci. Eng.* **2021**, *9*, 629. [CrossRef]

26. Bragg, W.H.; Bragg, W.L. The reflection of X-rays by crystals. *Nature* **1913**, *88*, 428–438. [CrossRef]

27. Mei, C.C.; Hara, T.; Naciri, M. Note on Bragg scattering of water waves by parallel bars on the seabed. *J. Fluid Mech.* **1988**, *186*, 147–162. [CrossRef]

28. Kirby, J.T. A note on Bragg scattering of surface waves by sinusoidal bars. *Phys. Fluids A Fluid Dyn.* **1993**, *5*, 858861. [CrossRef]

29. Liu, H.-W.; Zeng, H.-D.; Huang, H.-D. Bragg resonant reflection of surface waves from deep water to shallow water by a finite array of trapezoidal bars. *Appl. Ocean Res.* **2020**, *94*, 101976. [CrossRef]

30. Hao, J.; Li, J.; Liu, S.; Wang, L. Wave amplification caused by Bragg resonance on parabolic-type topography. *Ocean Eng.* **2022**, *244*, 110442. [CrossRef]

31. Bailard, J.A.; de Vries, J.; Kirby, J.T.; Guza, R.T. Bragg Reflection Breakwater: A New Shore Protection Method? In Proceedings of the Coastal Engineering Proceedings, Delft, The Netherlands, 2–6 July 1990. [CrossRef]

32. Bailard James, A.; de Vies Jack, W.; Kirby James, T. Considerations in Using Bragg Reflection for Storm Erosion Protection. *J. Waterw.* **1992**, *118*, 62–74. [CrossRef]

33. Davies, A.; Heathershaw, A. Surface-wave propagation over sinusoidally varying topography. *J. Fluid Mech.* **1984**, *144*, 419–443. [CrossRef]

34. Kirby, J.T. A general wave equation for waves over rippled beds. *J. Fluid Mech.* **1986**, *162*, 171–186. [CrossRef]

35. Mei, C.C. Resonant reflection of surface water waves by periodic sandbars. *J. Fluid Mech.* **1985**, *152*, 315–335. [CrossRef]

36. Kar, P.; Koley, S.; Sahoo, T. Scattering of surface gravity waves over a pair of trenches. *Appl. Math. Model.* **2018**, *62*, 303–320. [CrossRef]

37. Kar, P.; Koley, S.; Sahoo, T. Bragg scattering of long waves by an array of trenches. *Ocean Eng.* **2020**, *198*, 107004. [CrossRef]

38. Kar, P.; Sahoo, T.; Behera, H. Effect of Bragg scattering due to bottom undulation on a floating dock. *Wave Motion* **2019**, *90*, 121–138. [CrossRef]

39. Kar, P.; Sahoo, T.; Meylan, M.H. Bragg scattering of long waves by an array of floating flexible plates in the presence of multiple submerged trenches. *Phys. Fluids* **2020**, *32*, 096603. [CrossRef]

40. Ting, C.-L.; Lin, M.-C.; Kuo, C.-L. Bragg scattering of surface waves over permeable rippled beds with current. *Phys. Fluids* **2000**, *12*, 1382–1388. [CrossRef]

41. Xie, J.-J. Long wave reflection by an array of submerged trapezoidal breakwaters on a sloping seabed. *Ocean Eng.* **2022**, *252*, 111138. [CrossRef]

42. Tsai, C.-C.; Chou, W.-R. Comparison between consistent coupled-mode system and eigenfunction matching method for solving water wave scattering. *J. Mar. Sci. Technol.* **2015**, *23*, 870–881. [CrossRef]

43. Sahoo, T.; Chan, A.T.; Chwang, A.T. Scattering of oblique surface waves by permeable barriers. *J. Waterw.* **2000**, *126*, 196–205. [CrossRef]

44. Cho, Y.-S.; Yoon, S.B.; Lee, J.-I.; Yoon, T.-H. A concept of beach protection with submerged breakwaters. *J. Coast. Res.* **2001**, *34*, 671–678.

45. Tsai, C.-C.; Lin, Y.-T.; Chang, J.-Y.; Hsu, T.-W. A coupled-mode study on weakly viscous Bragg scattering of surface gravity waves. *Ocean Eng.* **2016**, *122*, 136–144. [CrossRef]

46. Kirby, J.T.; Anton, J.P. Bragg reflection of waves by artifical bars. In Proceedings of the 22nd International Conference on Coastal Engineering, ICCE'90, Delft, The Netherlands, 29 January 1990. [CrossRef]

47. Kaligatla, R.B.; Tabssum, S.; Sahoo, T. Effect of bottom topography on wave scattering by multiple porous barriers. *Meccanica* **2018**, *53*, 887–903. [CrossRef]
48. Chwang, A.T. A porous-wavemaker theory. *J. Fluid Mech.* **1983**, *132*, 395–406. [CrossRef]